J. Fluid Mech. (2016), *vol.* 796, *pp.* 659–711. © Cambridge University Press 2016
doi:10.1017/jfm.2016.227

The effect of Reynolds number on inertial particle dynamics in isotropic turbulence. Part 2. Simulations with gravitational effects

Peter J. Ireland[1,2], Andrew D. Bragg[1,2,‡] and Lance R. Collins[1,2,†]

[1]Sibley School of Mechanical and Aerospace Engineering, Cornell University, Ithaca, NY 14853, USA
[2]International Collaboration for Turbulence Research

(Received 23 July 2015; revised 18 January 2016; accepted 26 March 2016;
first published online 11 May 2016)

In Part 1 of this study (Ireland *et al.*, *J. Fluid Mech.*, vol. 796, 2016, pp. 617–658), we analysed the motion of inertial particles in isotropic turbulence in the absence of gravity using direct numerical simulation (DNS). Here, in Part 2, we introduce gravity and study its effect on single-particle and particle-pair dynamics over a wide range of flow Reynolds numbers, Froude numbers and particle Stokes numbers. The overall goal of this study is to explore the mechanisms affecting particle collisions, and to thereby improve our understanding of droplet interactions in atmospheric clouds. We find that the dynamics of heavy particles falling under gravity can be artificially influenced by the finite domain size and the periodic boundary conditions, and we therefore perform our simulations on larger domains to reduce these effects. We first study single-particle statistics that influence the relative positions and velocities of inertial particles. We see that gravity causes particles to sample the flow more uniformly and reduces the time particles can spend interacting with the underlying turbulence. We also find that gravity tends to increase inertial particle accelerations, and we introduce a model to explain that effect. We then analyse the particle relative velocities and radial distribution functions (RDFs), which are generally seen to be independent of Reynolds number for low and moderate Kolmogorov-scale Stokes numbers St. We see that gravity causes particle relative velocities to decrease by reducing the degree of preferential sampling and the importance of path-history interactions, and that the relative velocities have higher scaling exponents with gravity. We observe that gravity has a non-trivial effect on clustering, acting to decrease clustering at low St and to increase clustering at high St. By considering the effect of gravity on the clustering mechanisms described in the theory of Zaichik & Alipchenkov (*New J. Phys.*, vol. 11, 2009, 103018), we provide an explanation for this non-trivial effect of gravity. We also show that when the effects of gravity are accounted for in the theory of Zaichik & Alipchenkov (2009), the results compare favourably with DNS. The relative velocities and RDFs exhibit considerable anisotropy at small separations, and this anisotropy is quantified using spherical harmonic functions. We use the relative velocities and the RDFs to compute the particle collision kernels, and find that the collision kernel remains as it was for the case without gravity, namely nearly independent of Reynolds number for low and

† Email address for correspondence: lc246@cornell.edu
‡ Present address: Applied Mathematics and Plasma Physics Group, Los Alamos National Laboratory, Los Alamos, NM 87545, USA.

https://doi.org/10.1017/jfm.2016.227 Published online by Cambridge University Press

moderate *St*. We conclude by discussing practical implications of the results for the cloud physics and turbulence communities and by suggesting possible avenues for future research.

Key words: isotropic turbulence, particle/fluid flow, turbulent flows

1. Introduction

This is the second part of a two-part paper in which we consider the Reynolds-number dependence of inertial particle statistics using direct numerical simulations (DNS) of homogeneous, isotropic turbulence (HIT). In Part 1 of this study (Ireland, Bragg & Collins 2016), we used high-Reynolds-number DNS to explore the motion of inertial particles in the absence of gravity. We saw that particles with weak inertia preferentially sampled certain regions of the turbulence (a phenomenon known as 'preferential sampling', see Maxey 1987; Squires & Eaton 1991; Eaton & Fessler 1994). By exploring the specific regions of the flow contributing to this preferential sampling and using the theory in Chun *et al.* (2005), we were able to understand and model the resulting trends. Particles with higher inertia had a modulated response to the underlying turbulence (a phenomenon known as 'inertial filtering'), decreasing the particle kinetic energies and accelerations, and we found our DNS data for these quantities to be in excellent agreement with the models of Abrahamson (1975) and Zaichik & Alipchenkov (2008). Such particles also exhibited increased relative velocities and 'caustics' (Wilkinson & Mehlig 2005; Wilkinson, Mehlig & Bezuglyy 2006), which occur as a result of the particles' memory of their path-history interactions with the turbulence.

A primary goal of our analysis in Part 1 was to determine the effect of Reynolds number on particle collision rates. It is well known that droplet growth and precipitation in warm, cumulus clouds occur faster than current microphysical models can predict, and the discrepancies are generally linked to turbulence effects (see Shaw 2003; Devenish *et al.* 2012; Grabowski & Wang 2013). We explored droplet motions in turbulence at the highest Reynolds numbers to date, and used the results to extrapolate to Reynolds numbers representative of those in atmospheric clouds. A secondary motivation was to understand the extent to which protoplanetary nebula formation, which depends on the collision and coalescence of small dust grains, is affected by turbulence. (A more complete explanation of the physical processes involved in cloud and protoplanetary nebula formation is provided in Part 1.)

To determine the collision rates, we computed particle radial distributions and relative velocities and used the theory of Sundaram & Collins (1997) to calculate the kinematic collision kernel from these quantities. We observed that the collision rates of weakly inertial particles (such as those that would be present in the early stage of cloud formation) are almost entirely insensitive to the flow Reynolds number. This suggests that particle collisions are determined by the small-scale turbulence (and are insensitive to intermittency effects, which increase with increasing Reynolds number), and that DNS at low Reynolds numbers should capture the essential physics responsible for particle collisions in highly turbulent clouds.

One major simplification in Part 1 was the neglect of gravitational forces on the particles. However, as noted in Part 1, gravity is not negligible for many particle-laden environmental flows. For example, in warm cumulus clouds, the gravitational settling

https://doi.org/10.1017/jfm.2016.227 Published online by Cambridge University Press

speeds of droplets may be an order of magnitude larger than the Kolmogorov velocity, suggesting that such droplets fall quickly through the turbulence and may therefore have a substantially modified response to the underlying flow (Ayala *et al.* 2008). Therefore, in Part 2 of our study, we systematically explore the effect of gravity on inertial particle statistics.

The inclusion of gravity, while superficially trivial, adds richness and complexity to both the physical interpretation of the results as well as the numerics. Physically, the dimensionality of the parameter space is augmented by one to quantify the strength of gravity relative to the turbulence parameters. Here, we introduce a Froude number, Fr, which is defined as the ratio of the root-mean-square of the fluid acceleration to the gravitational constant (e.g. see Bec, Homann & Ray 2014). Even for terrestrial clouds (for which gravity may be regarded as a constant), the turbulent acceleration may vary by orders of magnitude (see Pruppacher & Klett 1997), leading to significant variations in Fr. To quantify the role of gravity, therefore, we must analyse particle statistics over a wide range of St, R_λ and Fr. In addition to the expanded parameter space, the gravitational vector causes a reduction in symmetry for the particle field, from isotropic to axisymmetric, with the axis aligned with the gravitational vector (Ayala *et al.* 2008; Woittiez, Jonker & Portela 2009; Bec *et al.* 2014; Gustavsson, Vajedi & Mehlig 2014). We will investigate the degree of anisotropy as a function of the system parameters. Finally, there is a numerical concern that relates to the settling speed of the particles. With periodic boundary conditions, particles exiting the bottom of the box are reintroduced at the top. If the time required to traverse the box becomes smaller than the correlation time of the turbulence, the reflected particles' pre-existing correlation with the flow will introduce an unphysical effect (Woittiez *et al.* 2009). This effect can be mitigated by increasing the domain size. We will explore different domain sizes to quantify this effect (see appendix A for a complete discussion).

Previous DNS of inertial particles subjected to gravity have primarily focused on how turbulence alters the terminal velocity (Wang & Maxey 1993; Yang & Lei 1998; Yang & Shy 2005; Ireland & Collins 2012; Bec *et al.* 2014; Good *et al.* 2014) and the collision frequency (Franklin, Vaillancourt & Yau 2007; Ayala *et al.* 2008; Onishi, Takahashi & Komori 2009; Woittiez *et al.* 2009; Rosa *et al.* 2013; Bec *et al.* 2014). Our work extends those studies by performing simulations on larger domains, over a wider range of Reynolds numbers and using more particle classes. We also consider the effect of gravity on additional particle statistics (such as fluid velocity gradients, Lagrangian time scales and particle accelerations) to provide new insight into the physical mechanisms responsible for particle collisions, and we specifically address the influence of anisotropy on these and other statistics. To understand the trends in many of these statistics, we introduce theoretical models and compare them with the DNS data.

The organization of this paper is as follows. In § 2, we discuss the numerical methods and parameters for our simulations. Single-particle statistics are presented in § 3. Within this section, we analyse particle velocity gradients (§ 3.1), mean settling speeds (§ 3.2) and accelerations (§ 3.3). These statistics provide insight into the mechanisms contributing to the clustering and near-contact motion of heavy, inertial particles. To further understand these and other relevant collision mechanisms, we directly compute particle-pair statistics in § 4. We consider the particle relative velocities in § 4.1 and radial distribution functions in § 4.2, and use these data to compute the particle kinematic collision kernel in § 4.3. We conclude in § 5 by summarizing our findings and suggesting some practical implications for the cloud physics and turbulence communities.

https://doi.org/10.1017/jfm.2016.227 Published online by Cambridge University Press

2. Overview of simulations

2.1. *Fluid phase*

As in Part 1, we perform pseudospectral DNS of HIT on a cubic, triperiodic domain of length $\mathscr{L}$ with N^3 grid points, solving the continuity and Navier–Stokes equations for an incompressible flow

$$\boldsymbol{\nabla}\cdot\boldsymbol{u}=0, \tag{2.1}$$

$$\frac{\partial \boldsymbol{u}}{\partial t}+\boldsymbol{\omega}\times\boldsymbol{u}+\boldsymbol{\nabla}\left(\frac{p}{\rho_f}+\frac{u^2}{2}\right)=\nu\nabla^2\boldsymbol{u}+\boldsymbol{f}, \tag{2.2}$$

where $\boldsymbol{u}$ is the fluid velocity, $\boldsymbol{\omega}$ is the vorticity, p is the pressure, ρ_f is the fluid density, ν is the kinematic viscosity and $\boldsymbol{f}$ is a large-scale forcing term that is added to make the flow field statistically stationary. In these simulations, deterministic forcing is applied to wavenumbers with magnitude $\kappa=\sqrt{2}$. Note that the gravity term in the Navier–Stokes equation is not shown because it is precisely cancelled by the mean pressure gradient, and so it has no dynamical consequence on the turbulent flow field. More details of the numerical methods can be found in Ireland *et al.* (2013).

In Part 1, $\mathscr{L}=2\pi$ for all the simulations performed. To reduce artificial periodicity effects in these simulations with gravity, the domain lengths are here extended to $\mathscr{L}=16\pi$ (for $R_\lambda=90$), $\mathscr{L}=8\pi$ (for $R_\lambda=147$) and $\mathscr{L}=4\pi$ (for $R_\lambda=230$). ($R_\lambda\equiv 2k\sqrt{5/(3\nu\epsilon)}$ denotes the Taylor-scale Reynolds number, where k is the kinetic energy and ϵ is the turbulent energy dissipation rate.) The grid spacing is kept constant as the domain size is increased, and so the small-scale resolution $\kappa_{max}\eta$ is approximately constant between the different domain sizes (where κ_{max} is the maximum resolved wavenumber and $\eta\equiv(\nu^3/\epsilon)^{1/4}$ is the Kolmogorov length scale). In increasing the domain size, we also keep the viscosity and forcing parameters the same, and thus both small-scale and large-scale flow parameters are held approximately constant. At the two highest Reynolds numbers, we expect periodicity effects to be minimal, and the domain sizes are the same ($\mathscr{L}=2\pi$) both with and without gravity. Refer to appendix A for a detailed examination of the effect of the domain size on fluid and particle statistics.

The simulation parameters are given in table 1. The simulation results from this study will be frequently compared to those from Part 1. These comparisons are justified, since in all cases, the parameters are very close to those used in Part 1, and based on the results in appendix A, we can safely assume that the differences in the particle statistics between these simulations and those in Part 1 are due entirely to gravitational effects and not to any differences in the underlying flow fields. In showing comparisons between the present data and those from Part 1, we will refer to both fields by the Reynolds numbers from table 1, keeping in mind that the corresponding Reynolds numbers from Part 1 may differ slightly (but by no more than 5 %).

To perform a more complete parametric study of the effects of inertia and gravity on particle statistics, we also conducted a simulation with similar flow parameters to simulation III, but with a smaller domain size (due to computational limitations). The parameters for this simulation (referred to as IIIb) are also given in table 1.

2.2. *Particle phase*

We simulate the motion of spherical particles with finite inertia and gravitational forces. To model the dynamics of inertial particles, we make the following simplifying assumptions. The particles are assumed to be small ($d/\eta\ll 1$, where d is the particle

https://doi.org/10.1017/jfm.2016.227 Published online by Cambridge University Press

Simulation	I	II	III	IV	V	IIIb
R_λ	90	147	230	398	597	227
$\mathscr{L}$	16π	8π	4π	2π	2π	2π
ν	0.005	0.002	0.0008289	0.0003	0.00013	0.0008289
ϵ	0.257	0.244	0.239	0.223	0.228	0.246
ℓ	1.47	1.44	1.49	1.45	1.43	1.43
ℓ/η	55.6	107	213	436	812	206
u'	0.912	0.914	0.914	0.915	0.915	0.915
u'/u_η	4.82	6.15	7.70	10.1	12.4	7.65
$\kappa_{max}\eta$	1.61	1.63	1.68	1.60	1.70	1.67
N	1024	1024	1024	1024	2048	512

TABLE 1. Simulation parameters for the DNS study. All dimensional parameters are in arbitrary units, and all quantities are defined in the text in §§ 2.1 and 2.2.

diameter) and dense ($\rho_p/\rho_f \gg 1$, where ρ_p is the particle density). As in Part 1, we assume the leading-order force acting on the particles is Stokes drag, which is justified when the particle Reynolds number $Re_p \equiv |\boldsymbol{u}^p(t) - \boldsymbol{v}^p(t)|/\nu < 0.5$, where $\boldsymbol{u}^p(t) \equiv \boldsymbol{u}(\boldsymbol{x}^p(t), t)$ denotes the undisturbed fluid velocity at the particle position $\boldsymbol{x}^p$ and $\boldsymbol{v}^p$ denotes the velocity of the particle (Elghobashi & Truesdell 1992). (As in Part 1, we use the superscript p on $\boldsymbol{x}$, $\boldsymbol{u}$ and $\boldsymbol{v}$ to denote time-dependent Lagrangian variables defined along particle trajectories. Phase-space positions and velocities will be denoted without the superscript p.) In a recent study, Good *et al.* (2014) found that the linear drag model (Stokes drag) predicted settling speeds in agreement with experiments for $St \lesssim 3$; however, for $St > 3$ the linear drag model yields results that are inconsistent with experiments. However, simply introducing a nonlinear drag coefficient does not quantitatively capture the nonlinear drag effects in a time-dependent flow like turbulence. A full wake-resolving nonlinear model would be required, but is beyond the scope of this study. Despite the need for caution in the interpretation of the higher-Stokes-number simulations, the majority of DNS and theory derived for particle-laden flows also assume a linear drag law, and hence we retain a linear drag model in this study to facilitate comparisons with the earlier work. A future study will consider a more general drag law in conjunction with experimental measurements to test the model. Finally, we neglect interparticle interactions and two-way coupling between the phases under the assumption that the particle loadings are in the dilute limit (Elghobashi & Truesdell 1993; Sundaram & Collins 1999), as is typically the case in atmospheric clouds (Shaw 2003).

Under these assumptions, the governing equations for the inertial particles are (Maxey & Riley 1983)

$$\frac{\mathrm{d}^2\boldsymbol{x}^p}{\mathrm{d}t^2} = \frac{\mathrm{d}\boldsymbol{v}^p}{\mathrm{d}t} = \frac{\boldsymbol{u}\,(\boldsymbol{x}^p(t), t) - \boldsymbol{v}^p(t)}{\tau_p} + \mathfrak{g}, \tag{2.3}$$

where $\mathfrak{g} = (0, 0, -\mathfrak{g})$ is the gravitational acceleration vector and $\tau_p \equiv \rho_p d^2/(18\rho_f\nu)$ is the response time of the particle. To compute $\boldsymbol{u}(\boldsymbol{x}^p(t), t)$, we employ an eight-point B-spline interpolation from the Eulerian grid (van Hinsberg *et al.* 2012). As in Part 1, we begin computing particle statistics once the particle distributions and velocities become statistically stationary and independent of their initial conditions. For a subset $N_{tracked}$ of the total number of particles in each class N_p, we store particle positions,

https://doi.org/10.1017/jfm.2016.227 Published online by Cambridge University Press

velocities and velocity gradients every $0.1\tau_\eta$ for a duration of approximately $100\tau_\eta$. These data are used to compute Lagrangian correlations, accelerations and time scales.

The Stokes number $St \equiv \tau_p/\tau_\eta$ is a non-dimensional measure of the particle inertia, where $\tau_\eta \equiv (\nu/\epsilon)^{1/2}$ is the Kolmogorov time scale. Gravity can be parameterized in a number of ways (e.g. see Good *et al.* 2014). Here, we define the Froude number as $Fr \equiv \epsilon^{3/4}/(\nu^{1/4}\mathrm{g})$, where $\epsilon^{3/4}/\nu^{1/4}$ is the Kolmogorov estimate for the acceleration root-mean-square. (Note that the Froude number is sometimes expressed as the inverse of our definition; we choose the present definition for consistency with the standard practice of defining the Froude number with g in the denominator.) Alternatively, gravity can be parameterized by the settling parameter $Sv \equiv \tau_p\mathrm{g}/u_\eta$, which is the ratio of the particle's settling velocity $\tau_p\mathrm{g}$ to the Kolmogorov velocity of the turbulence $u_\eta \equiv (\nu\epsilon)^{1/4}$. Note that these two non-dimensional parameters are related through the Stokes number, $Fr = St/Sv$, and that the Froude number Fr is independent of τ_p.

Since a primary aim of this paper is to study the effect of gravity at conditions representative of those in cumulus clouds, we calculate Fr and Sv by assuming a dissipation rate $\epsilon = 10^{-2}$ m^2 s^{-3} (Shaw 2003), a kinematic viscosity $\nu = 1.5 \times 10^{-5}$ m^2 s^{-1} and a gravitational acceleration $\mathrm{g} = 9.8$ m s^{-2}, yielding $Fr = 0.052$ or $Sv = 19.3St$. Simulations I, II, III and IV were run with $Fr = 0.052$ and particles with Stokes numbers in the range $0 \leqslant St \leqslant 3$; due to computational limitations, simulation V was only run with $0 \leqslant St \leqslant 0.3$.

Experimental observations suggest that cloud dissipation rates can vary by orders of magnitude (e.g. see Pruppacher & Klett 1997), resulting in commensurate variations in Fr and Sv. For example, a strongly turbulent cumulonimbus cloud with $\epsilon \sim 10^{-1}$ m^2 s^{-3} yields $Fr \approx 0.3$ and $Sv \approx 3.4St$, while a weakly turbulent stratiform cloud with $\epsilon \sim 10^{-3}$ m^2 s^{-3} yields $Fr \approx 0.01$ and $Sv \approx 100St$ (Pinsky, Khain & Shapiro 2007). To study a larger St–Sv parameter space, we analysed 513 different combinations of St and Sv in simulation IIIb, with $0 \leqslant St \leqslant 56.2$ and $0 \leqslant Sv \leqslant 100$. The results from this simulation will be used to study detailed trends in particle accelerations, clustering, relative velocities and collision rates for different values of particle inertia and gravity. (The trends in the particle kinetic energies and settling velocities obtained from this data set are discussed in detail in Good *et al.* (2014).)

3. Single-particle statistics

As in Part 1, we begin with the statistics of individual inertial particles. We present velocity gradient statistics in § 3.1, gravitational settling velocity statistics in § 3.2 and acceleration statistics in § 3.3.

3.1. *Velocity gradient statistics*

We begin by considering velocity gradients sampled along inertial particle trajectories, here denoted by $\boldsymbol{A}(\boldsymbol{x}^p(t), t) \equiv \boldsymbol{\nabla u}(\boldsymbol{x}^p(t), t)$. These statistics affect the relative motion of particles with weak-to-moderate inertia with separations in the dissipation range, and also quantify the degree to which the inertial particles preferentially sample the underlying turbulence (e.g. see Chun *et al.* 2005). This information will prove useful in interpreting the relative velocity and clustering statistics presented in §§ 4.1 and 4.2. It is convenient to define the rate-of-strain and rate-of-rotation tensors as $\boldsymbol{S}(\boldsymbol{x}^p(t), t) \equiv [\boldsymbol{A}(\boldsymbol{x}^p(t), t) + \boldsymbol{A}^{\mathrm{T}}(\boldsymbol{x}^p(t), t)]/2$ and $\boldsymbol{R}(\boldsymbol{x}^p(t), t) \equiv [\boldsymbol{A}(\boldsymbol{x}^p(t), t) - \boldsymbol{A}^{\mathrm{T}}(\boldsymbol{x}^p(t), t)]/2$, respectively.

We first consider the variance of the diagonal components of $\boldsymbol{S}$ averaged along the particle trajectories. For fluid particles that uniformly sample the flow, their variances reduce to $\langle[S_{11}(\boldsymbol{x}^p(t), t)]^2\rangle = \langle[S_{22}(\boldsymbol{x}^p(t), t)]^2\rangle = \langle[S_{33}(\boldsymbol{x}^p(t), t)]^2\rangle = 1/(15\tau_\eta^2)$. In isotropic

https://doi.org/10.1017/jfm.2016.227 Published online by Cambridge University Press

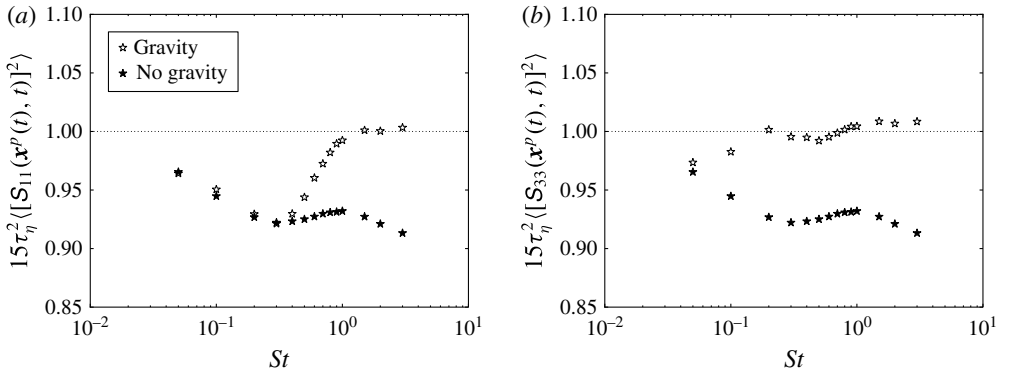

FIGURE 1. The normalized variance of the diagonal components of the rate-of-strain tensor sampled by inertial particles for different values of St at $R_\lambda = 398$. Open symbols denote data with gravity ($Fr = 0.052$) and filled symbols denote data without gravity ($Fr = \infty$). The horizontal dotted line indicates the expected value for uniformly distributed particles in isotropic turbulence. The gradients in the horizontal and vertical directions are shown in (*a*) and (*b*), respectively.

turbulence without gravity, these components are statistically equivalent; however, in the presence of gravity, the symmetry of the particle motion is reduced from isotropic to axisymmetric, and thus the statistics of $\boldsymbol{S}$ along the direction of gravity, x_3, will differ from the transverse directions, x_1 and x_2. For the remainder of the paper, the x_3 direction will be denoted as the 'vertical' direction and the x_1 and x_2 directions will be referred to as the 'horizontal' directions. The data for the two horizontal directions will be averaged together whenever possible, and denoted with the subscript '1'.

Figure 1 shows the variance of (*a*) horizontal ($\langle S_{11}^2\rangle^p \equiv \langle[S_{11}(\boldsymbol{x}^p(t),\, t)]^2\rangle$) and (*b*) vertical ($\langle S_{33}^2\rangle^p \equiv \langle[S_{33}(\boldsymbol{x}^p(t),\, t)]^2\rangle$) components of the rate-of-strain tensor as a function of St, both with gravity ($Fr = 0.052$) and without gravity ($Fr = \infty$). Without gravity, the strain rates decrease with increasing St for $St \lesssim 0.3$. This is closely related to the trend in the strain rates observed in Part 1, which was attributed to the fact that inertia causes particles to be ejected from vortex sheets. With gravity, the strain rates in the horizontal direction also decrease with increasing St for $St \lesssim 0.3$, as seen in figure 1(*a*). In addition, they are quite close to the corresponding values without gravity, suggesting that gravity does not lead to significant changes in preferential sampling in the horizontal direction at low St. We see in figure 1(*b*), however, that gravity causes low-St particles to sample regions of larger vertical strain rates, and that these strain rates are considerably different from those when gravity is absent. We also observe that gravity reduces the degree of preferential sampling at high St, causing the strain rates to approach the values predicted for uniformly distributed particles in isotropic turbulence for $St \gtrsim 1$.

In figure 2, we plot $\tau_\eta^2\langle S^2\rangle^p$, $\tau_\eta^2\langle R^2\rangle^p$, and $\tau_\eta^2(\langle S^2\rangle^p - \langle R^2\rangle^p)$, where $\langle S^2\rangle^p \equiv \langle \boldsymbol{S}(\boldsymbol{x}^p(t),\, t) : \boldsymbol{S}(\boldsymbol{x}^p(t),\, t)\rangle$ and $\langle R^2\rangle^p \equiv \langle \boldsymbol{R}(\boldsymbol{x}^p(t),\, t) : \boldsymbol{R}(\boldsymbol{x}^p(t),\, t)\rangle$ are the second invariants of the rate-of-strain and rate-of-rotation tensors, respectively, for particles with ($Fr = 0.052$) and without ($Fr = \infty$) gravity. As noted in Part 1, when preferential sampling effects are absent, $\tau_\eta^2\langle S^2\rangle^p = \tau_\eta^2\langle R^2\rangle^p = 0.5$. We see from figure 2 that gravity reduces the degree of preferential sampling, causing $\tau_\eta^2\langle S^2\rangle^p$, $\tau_\eta^2\langle R^2\rangle^p$, and $\tau_\eta^2(\langle S^2\rangle^p - \langle R^2\rangle^p)$ to be closer to the corresponding values for uniformly distributed

https://doi.org/10.1017/jfm.2016.227 Published online by Cambridge University Press

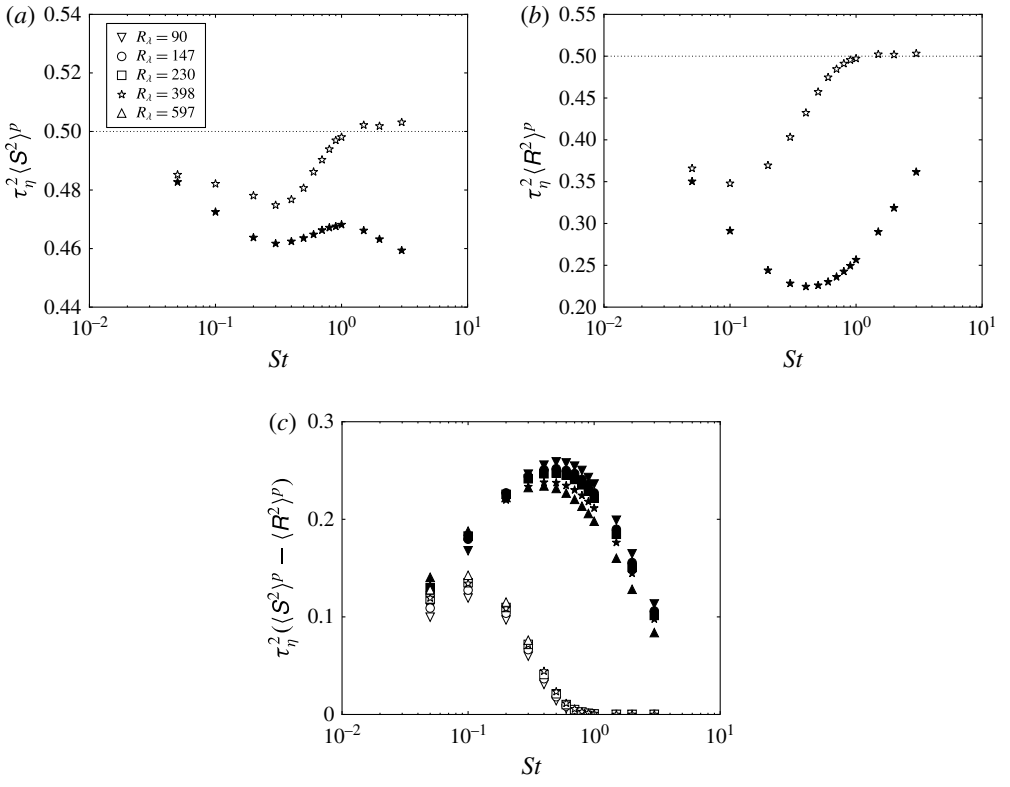

FIGURE 2. $\langle S^2\rangle^p$ (*a*), $\langle R^2\rangle^p$ (*b*) and $\langle S^2\rangle^p - \langle R^2\rangle^p$ (*c*) as function of *St*. Open symbols denote data with gravity ($Fr = 0.052$) and filled symbols denote data without gravity ($Fr = \infty$). To improve the readability of the plots, data are only shown for $R_\lambda = 398$ in (*a*,*b*). Data at all values of R_λ are included in (*c*).

particles. We also note that preferential sampling effects are eliminated altogether for $St \gtrsim 1$, which is consistent with the results presented earlier. The trends in the mean strain and rotation rates with R_λ are not shown in figure 2(*a*,*b*) to improve the readability of the plots, but are similar both with and without gravity and are discussed in Part 1.

To explain the reduction in preferential sampling with gravity, we note that gravity, by causing particles to settle relative to the underlying flow, reduces the interaction times between the particles and the turbulent eddies. As a result, particles have less time to be affected by the straining and rotating regions of the flow and therefore experience less preferential sampling (see also Gustavsson *et al.* 2014).

We test this argument by computing Lagrangian rate-of-strain and rate-of-rotation time scales along inertial particle trajectories, both with and without gravity. These time scales will prove useful for extending the theoretical model of Zaichik & Alipchenkov (2009) to account for gravitational effects. Their model, developed for an isotropic particle field, uses a single time scale for the rate-of-strain tensor and a single time scale for the rate-of-rotation tensor. To generalize the model for the case with gravity, directionally dependent times scales are required. We discuss the generalized model and its comparison with DNS in § 4.2.

https://doi.org/10.1017/jfm.2016.227 Published online by Cambridge University Press

(1)	$T^p_{S_{11}S_{11}}$	$T^p_{S_{22}S_{22}}$
(2)	$T^p_{S_{11}S_{22}}$	
(3)	$T^p_{S_{12}S_{12}}$	
(4)	$T^p_{S_{13}S_{13}}$	$T^p_{S_{23}S_{23}}$
(5)	$T^p_{S_{11}S_{33}}$	$T^p_{S_{22}S_{33}}$
(6)	$T^p_{S_{33}S_{33}}$	
(1)	$T^p_{R_{12}R_{12}}$	
(2)	$T^p_{R_{13}R_{13}}$	$T^p_{R_{23}R_{23}}$

TABLE 2. Categorization of the strain and rotation time scales with gravity. (Gravity is aligned with the x_3-direction.) The elements within a given row are statistically equivalent, while the elements in different rows may differ due to the anisotropy in the particle motion.

We consider both the Lagrangian strain time scale $T^p_{S_{ij}S_{km}}$, which we define as

$$T^p_{S_{ij}S_{km}} \equiv \frac{\displaystyle\int_0^\infty \left\langle S_{ij}(\boldsymbol{x}^p(0),0)S_{km}(\boldsymbol{x}^p(s),s)\right\rangle \,\mathrm{d}s}{\left\langle S_{ij}(\boldsymbol{x}^p(0),0)S_{km}(\boldsymbol{x}^p(0),0)\right\rangle}, \tag{3.1}$$

and the Lagrangian rotation time scale $T^p_{R_{ij}R_{km}}$, defined as

$$T^p_{R_{ij}R_{km}} \equiv \frac{\displaystyle\int_0^\infty \left\langle R_{ij}(\boldsymbol{x}^p(0),0)R_{km}(\boldsymbol{x}^p(s),s)\right\rangle \,\mathrm{d}s}{\left\langle R_{ij}(\boldsymbol{x}^p(0),0)R_{km}(\boldsymbol{x}^p(0),0)\right\rangle}. \tag{3.2}$$

In both of these equations, no summation is implied by the repeated indices.

In the absence of gravity, the particle field is isotropic, which implies the rate-of-strain time scales $T^p_{S_{11}S_{11}}$, $T^p_{S_{11}S_{22}}$, $T^p_{S_{11}S_{33}}$, $T^p_{S_{12}S_{12}}$, $T^p_{S_{13}S_{13}}$, $T^p_{S_{22}S_{22}}$, $T^p_{S_{22}S_{33}}$, $T^p_{S_{23}S_{23}}$, and $T^p_{S_{33}S_{33}}$ are statistically equivalent, as are the rotation time scales $T^p_{R_{12}R_{12}}$, $T^p_{R_{13}R_{13}}$ and $T^p_{R_{23}R_{23}}$. However, with gravity, the nine rate-of-strain time scales are no longer equivalent, nor are the three rate-of-rotation time scales. Applying symmetry analysis, we can group the nine rate-of-strain time scales into six categories, and the three rate-of-rotation time scales into two categories, as shown in table 2. Additionally, we introduce T^p_{SS} and T^p_{RR} as the average of the nine rate-of-strain time scales and the three rate-of-rotation time scales, respectively.

Figure 3 shows the averaged time scales T^p_{SS} and T^p_{RR} as a function of the particle Stokes number at different values of R_λ, with and without gravity. In agreement with the physical explanations offered above, we see that the time scales without gravity always exceed those with gravity. We also note that both with and without gravity, the strain time scales are almost entirely insensitive to the Reynolds number. In addition, while the rate-of-rotation time scales without gravity vary weakly with R_λ (as noted in Part 1), they are nearly independent of the Reynolds number with gravity.

We now consider the anisotropy in the different time scales with gravity at $R_\lambda = 398$ in figure 4. In this plot, we have averaged together the statistically equivalent time scales grouped in table 2, and have denoted these time scales by the first (or only) item in these groups. We have not included data for cases without gravity, since

https://doi.org/10.1017/jfm.2016.227 Published online by Cambridge University Press

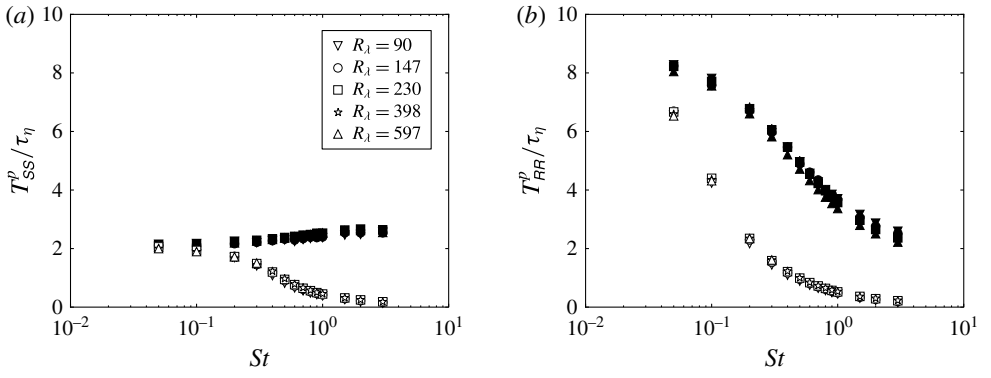

FIGURE 3. The averaged strain time scale T^p_{SS} (a) and the averaged rotation time scale T^p_{RR} (b) plotted as a function of St for different values of R_λ. Open symbols denote data with gravity ($Fr = 0.052$) and filled symbols denote data without gravity ($Fr = \infty$).

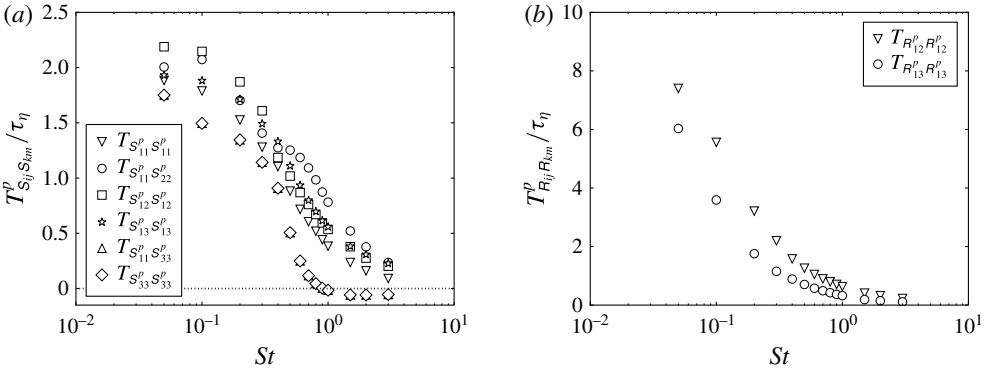

FIGURE 4. The Lagrangian strain (a) and rotation (b) time scales in different directions at $R_\lambda = 398$, plotted as a function of St, for particles with gravity ($Fr = 0.052$).

each of the time scales without gravity are statistically equivalent (as noted above), and would be identical to those presented in figure 3. As expected, the time scales show considerable anisotropy with gravity. If we consider the limit of strong gravity ($Sv \gg u'/u_\eta$), we can derive a simple model for the time scales (see appendix B for the derivation and estimates of droplet diameters required for the model to be valid in different atmospheric clouds). Using the relations in § B.1, the Lagrangian rate-of-strain and rate-of-rotation time scales take the form

$$\hat{T}^p_{S_{ij}S_{km}} = \frac{\hat{\ell}_{S_{ij}S_{km},3}}{Sv}, \tag{3.3}$$

and

$$\hat{T}^p_{R_{ij}R_{km}} = \frac{\hat{\ell}_{R_{ij}R_{km},3}}{Sv}, \tag{3.4}$$

respectively, where we have used the top-hat symbol to denote a variable normalized by Kolmogorov scales, and $\ell_{S_{ij}S_{km},3}$ ($\ell_{R_{ij}R_{km},3}$) is the integral length scale of $S_{ij}S_{km}$ ($R_{ij}R_{km}$) evaluated along the x_3-direction.

https://doi.org/10.1017/jfm.2016.227 Published online by Cambridge University Press

Equations (3.3) and (3.4) imply that in the limit $Sv \gg u'/u_\eta$, the Lagrangian integral time scales of the flow experienced by the particles are directly proportional to the Eulerian integral length scales of the strain and rotation fields. We can therefore write each of the Lagrangian time scales in table 2 as functions of their corresponding Eulerian integral length scales. This allows us to use tensor invariance theory and the properties of the strain and rotation rate tensors in HIT to predict the relative magnitude of the different time scales. We therefore can show that

$$T^p_{S_{11}S_{33}} = T^p_{S_{33}S_{33}} < T^p_{S_{11}S_{11}} < T^p_{S_{12}S_{12}} = T^p_{S_{13}S_{13}} < T^p_{S_{11}S_{22}}, \tag{3.5}$$

and

$$T^p_{R_{13}R_{13}} < T^p_{R_{12}R_{12}}. \tag{3.6}$$

The DNS data in figure 4 follow the trends predicted by (3.5) and (3.6) at high St.

3.2. *Mean particle settling velocities*

We now analyse the effect of turbulence on the mean settling speed of inertial particles. The role of the mean settling velocity, aside from its importance to the process of cloud rain out, is also related to the evolution of the droplet size distribution through its effect on the collision kernel of different-sized particles, as discussed in Dávila & Hunt (2001) and Ghosh *et al.* (2005) and later modelled by Grabowski & Wang (2013).

Recently, Good *et al.* (2014) measured settling speeds of particles in turbulence and showed that turbulence causes particles with low-to-moderate Stokes numbers to settle more quickly than they would in a quiescent fluid. The so-called 'preferential sweeping' or 'fast tracking' of particles (particles sampling downward-moving fluid over upward-moving fluid) had been observed in DNS (Wang & Maxey 1993; Yang & Lei 1998; Ireland & Collins 2012; Bec *et al.* 2014) and earlier experiments (Aliseda *et al.* 2002; Yang & Shy 2003, 2005). For $St \gtrsim 1$, Good *et al.* (2014) observed a transition to so-called 'loitering' (particles settling more slowly than they would in a quiescent fluid), again consistent with earlier experiments (Nielsen 1993; Yang & Shy 2003; Kawanisi & Shiozaki 2008), although Good *et al.* (2014) were the first to measure it for droplets in air. In contrast, DNS with linear drag shows preferential sweeping at all Stokes numbers, with no transition to loitering (Wang & Maxey 1993; Yang & Lei 1998; Ireland & Collins 2012; Bec *et al.* 2014). In order to observe loitering in DNS, the linear drag must be replaced by a nonlinear drag model (e.g. Clift, Grace & Weber 1978). The nonlinear drag model yields settling speeds that are only in qualitative, but not quantitative, agreement with the experiments, most likely due to the simplistic nature of the nonlinear drag model that was used (Good *et al.* 2014).

Here, we extend the range of Reynolds numbers for $0 \leqslant St \leqslant 3$ and $Fr = 0.052$ using a linear drag model. From (2.3) we can show that

$$\langle \boldsymbol{u}(\boldsymbol{x}^p(t), t)\rangle = \langle \boldsymbol{v}^p(t)\rangle - \tau_p \mathfrak{g} \equiv -\langle \boldsymbol{\Delta v}\rangle^p, \tag{3.7}$$

where $\tau_p \mathfrak{g} = (0, 0, -\tau_p g)^{\mathrm{T}}$ is the gravitational settling velocity in a quiescent flow. Preferential sweeping corresponds to $\langle \Delta v_3\rangle^p > 0$ and loitering to $\langle \Delta v_3\rangle^p < 0$. Figure 5 shows $\langle \Delta v_3\rangle^p$, normalized by the Kolmogorov velocity u_η, as a function of the particle Stokes number. Consistent with the DNS results presented in Good *et al.* (2014), the DNS with linear drag shows no significant loitering at any Reynolds number. (Note

https://doi.org/10.1017/jfm.2016.227 Published online by Cambridge University Press

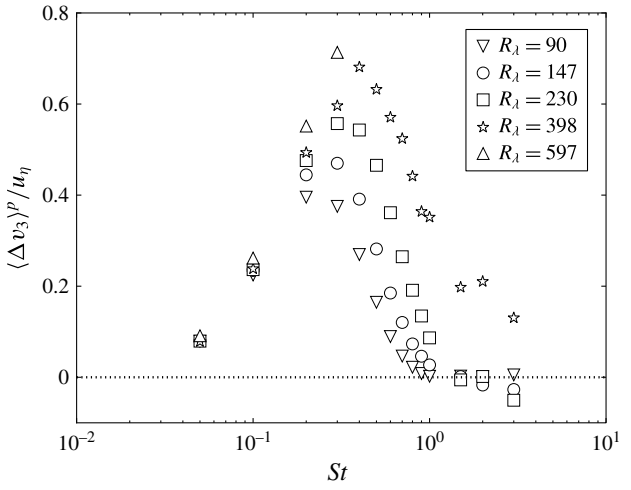

FIGURE 5. Turbulence-induced enhancements (positive) or reductions (negative) in the mean settling velocities of inertial particles with gravity ($Fr = 0.052$), normalized by the Kolmogorov velocity u_η. The symbols denote different values of R_λ.

that while the slight loitering observed at $St = 3$ for $R_\lambda = 147$ and $R_\lambda = 230$ is statistically significant, the quiescent settling velocity is reduced by less than 0.1 %, and thus the overall effect is negligible. In Good *et al.* (2014), the settling speed reductions with nonlinear drag were observed to be one to two orders of magnitude larger than this.) Moreover, we see that the mean settling speeds are independent of R_λ for $St \leqslant 0.1$, suggesting that in this limit, they are determined entirely by the small-scale turbulence, in agreement with Bec *et al.* (2014). At higher St, the settling speeds are stronger functions of the Reynolds number; however, these results must be interpreted with some caution given the concerns raised about linear drag in this regime. Nevertheless, we see at least the potential for a significant Reynolds-number effect on the mean settling velocities at higher Stokes number.

3.3. *Particle accelerations*

We now consider the acceleration statistics of the particles. As noted in Chun *et al.* (2005), the relative velocity of different-sized particles (and thus their collision rate) is related to their accelerations. Figure 6 shows the particle acceleration variances $\langle a_1^2 \rangle^p \equiv \langle (\mathrm{d}v_1^p(t)/\mathrm{d}t)^2 \rangle$ and $\langle a_3^2 \rangle^p \equiv \langle (\mathrm{d}v_3^p(t)/\mathrm{d}t)^2 \rangle$, with and without gravity. Notice that the acceleration variances with gravity always exceed those without gravity, in some cases by as much as an order of magnitude. Similar trends were observed in computational and experimental studies of channel flows (Gerashchenko *et al.* 2008; Lavezzo *et al.* 2010) and more recently in the computational study of Parishani *et al.* (2015) in HIT.

We also see that gravity reverses the trends in the particle accelerations at low St, causing the accelerations to increase with increasing St. This trend was recently reported in Parishani *et al.* (2015) at lower values of R_λ ($R_\lambda = 119$–143). Our results in appendix A, however, suggest that the acceleration statistics in Parishani *et al.* (2015), while qualitatively correct, have quantitative errors due the influence of artificial periodicity effects on the small domain sizes in their simulations. Experimental studies of inertial particle accelerations in HIT (Ayyalasomayajula *et al.* 2006) and

https://doi.org/10.1017/jfm.2016.227 Published online by Cambridge University Press

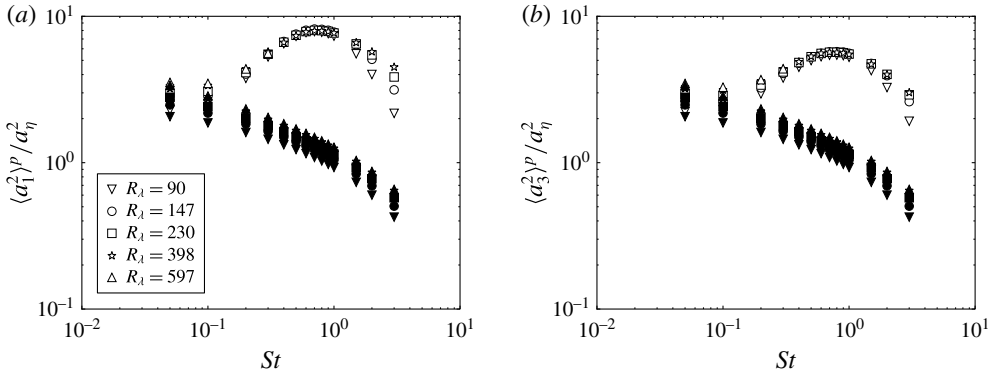

FIGURE 6. The variance of the particle accelerations in the horizontal (*a*) and vertical (*b*) directions. Open symbols denote data with gravity ($Fr = 0.052$), and filled symbols denote data without gravity ($Fr = \infty$).

Von Kármán flows (Volk *et al.* 2008*a*,*b*) have only observed a monotonic decrease of the particle accelerations with increasing St, presumably because the Froude numbers in those studies ($Fr \sim 0.3$ for HIT and $Fr \sim 30$ for the Von Kármán flow) were too large to observe this trend reversal. (Recall that in our study, $Fr = 0.052$.)

We now provide a physical explanation for these large accelerations. We begin by considering the limit $St \ll 1$. If gravitational forces are negligible, to leading order the particle acceleration $\boldsymbol{a}^p(t)$ is equivalent to the fluid acceleration at the particle location (e.g. see Bec *et al.* 2006)

$$\boldsymbol{a}^p(t) \approx \frac{\partial \boldsymbol{u}(\boldsymbol{x}^p(t), t)}{\partial t} + \boldsymbol{u}(\boldsymbol{x}^p(t), t) \cdot \boldsymbol{\nabla} \boldsymbol{u}(\boldsymbol{x}^p(t), t). \tag{3.8}$$

As the gravitational force increases (i.e. as Sv increases), it is the interplay between gravity and turbulence that determines the particle acceleration. For example, the downward drift due to the gravitational settling will cause the particle to experience different regions of the turbulence. We refer to this phenomenon as the 'gravitational trajectory effect'. (Note that Yudine (1959) coined 'crossing trajectories' to refer to the same mechanism.)

The particle acceleration in the limits $St \ll 1$ and $Sv \gg 1$ can be approximated by the derivative of the fluid velocity along the inertial particle trajectory (denoted here as $\mathrm{d}\boldsymbol{u}^p/\mathrm{d}t$), yielding (see Bec *et al.* 2006)

$$\boldsymbol{a}^p(t) \approx \frac{\mathrm{d}\boldsymbol{u}^p}{\mathrm{d}t} = \frac{\partial \boldsymbol{u}(\boldsymbol{x}^p(t), t)}{\partial t} + \boldsymbol{v}^p(t) \cdot \boldsymbol{\nabla} \boldsymbol{u}(\boldsymbol{x}^p(t), t). \tag{3.9}$$

We compare the variances of the horizontal and vertical components of $\mathrm{d}\boldsymbol{u}^p(t)/\mathrm{d}t$ (denoted as $\langle(\mathrm{d}u_1/\mathrm{d}t)^2\rangle^p$ and $\langle(\mathrm{d}u_3/\mathrm{d}t)^2\rangle^p$, respectively) with $\langle a_1^2\rangle^p$ and $\langle a_3^2\rangle^p$ in figure 7. The variances of $\boldsymbol{a}^p(t)$ and $\mathrm{d}\boldsymbol{u}^p(t)/\mathrm{d}t$ are almost identical at low St, as expected. As St increases, the particles have larger settling velocities, causing the fluid seen by the particles to change more rapidly in time. As a result, the variance of $\mathrm{d}\boldsymbol{u}^p/\mathrm{d}t$ increases monotonically without bound with increasing St. In contrast, the inertial particle acceleration peaks around $St \sim 1$ and then decreases, causing the variance of $\mathrm{d}\boldsymbol{u}^p/\mathrm{d}t$ to exceed that of $\boldsymbol{a}^p(t)$ for $St \gtrsim 0.3$. The trend for the acceleration

https://doi.org/10.1017/jfm.2016.227 Published online by Cambridge University Press

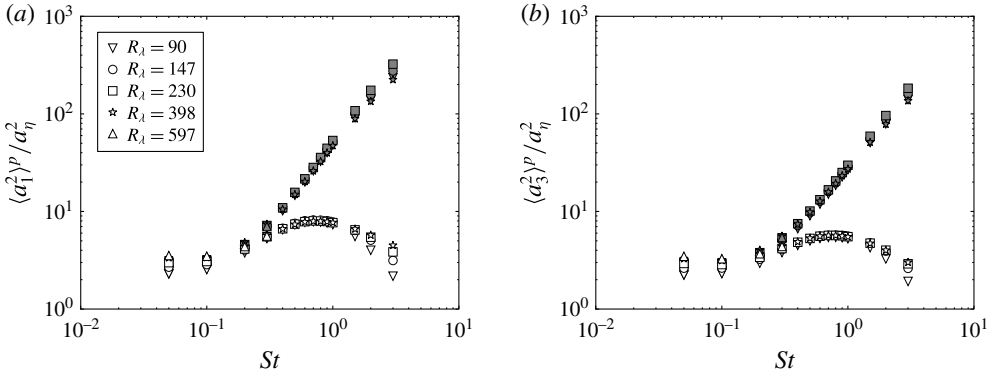

FIGURE 7. Inertial particle acceleration variances in the horizontal (a) and vertical (b) directions for different values of St and R_λ. All data are with gravity included ($Fr = 0.052$). Open symbols denote $\langle a_1^2 \rangle^p$ (a) and $\langle a_3^2 \rangle^p$ (b) and filled symbols denote $\langle (\mathrm{d}u_1/\mathrm{d}t)^2 \rangle^p$ (a) and $\langle (\mathrm{d}u_3/\mathrm{d}t)^2 \rangle^p$ (b).

variance occurs because the particle's inertia also modulates its response to the underlying fluid through 'inertial filtering' (Bec *et al.* 2006; Salazar & Collins 2012). The particle is unable to respond to fluid fluctuations with frequencies greater than $O(1/\tau_p)$, causing a reduction in the acceleration variance. Beyond $St \sim 1$, inertial filtering dominates the enhancement due to gravitational settling, causing the particle accelerations to decrease with increasing St.

Parishani *et al.* (2015) also observed a peak in the particle acceleration variance for $St \sim 1$ with gravity, and argued that the preferential sweeping mechanism identified in Wang & Maxey (1993) is responsible for producing these large accelerations. While we observe a similar peak in the acceleration variances, we find preferential sweeping to be negligible at $St \sim 1$ for $R_\lambda \lesssim 230$ (see § 3.2). Our data also indicate that the preferential sweeping of $St \sim 1$ particles varies significantly with R_λ, while the acceleration variances are nearly independent of R_λ. These findings suggest that preferential sweeping cannot fully explain the trends in the acceleration variances with gravity. In contrast, the approach we have taken is able to predict the dependence of the accelerations on St and Sv without appealing to preferential sweeping arguments.

By comparing figures 7(a) and 7(b) we notice that $\langle a_1^2 \rangle^p$ generally exceeds $\langle a_3^2 \rangle^p$. We use the acceleration model derived in § B.2 to explain this result in the limit $Sv \gg u'/u_\eta$. From § B.2, we have the following models for the particle acceleration variances in the high-Sv limit:

$$\frac{\langle a_1^2 \rangle^p}{a_\eta^2} = \left[\frac{u'}{u_\eta}\right]^2 \left[\frac{Sv}{St}\right] \left[\frac{2StSv + 3\left(\dfrac{\ell}{\eta}\right)}{2\left(StSv + \dfrac{\ell}{\eta}\right)^2}\right], \tag{3.10}$$

and

$$\frac{\langle a_3^2 \rangle^p}{a_\eta^2} = \left[\frac{u'}{u_\eta}\right]^2 \left[\frac{Sv}{St}\right] \left[\frac{1}{StSv + \dfrac{\ell}{\eta}}\right]. \tag{3.11}$$

https://doi.org/10.1017/jfm.2016.227 Published online by Cambridge University Press

By taking the ratio of (3.10) and (3.11), we see that

$$\frac{\langle a_1^2\rangle^p}{\langle a_3^2\rangle^p} = \frac{2StSv + 3\left(\dfrac{\ell}{\eta}\right)}{2StSv + 2\left(\dfrac{\ell}{\eta}\right)}, \tag{3.12}$$

and thus the model also predicts that $\langle a_1^2\rangle^p$ exceeds $\langle a_3^2\rangle^p$ by an amount that increases with R_λ.

In the derivation of this model, we assumed that the particles' primary motion is in the vertical direction, from which it followed that the particle accelerations were related to the correlation length scales of the fluid velocities sampled along the particle trajectories. Since in isotropic turbulence the longitudinal integral length scale is twice the transverse integral length scale, the particles (as they fall vertically) will experience vertical fluid velocities that are more strongly correlated over a time τ_p than are the horizontal fluid velocities. (This phenomenon was referred to as the 'continuity effect' in Csanady (1963), and is also explained in Yudine (1959) and Good *et al.* (2014).) As a result, the horizontal fluid velocities sampled by the particles will change more rapidly, leading to larger particle accelerations in those directions.

In Parishani *et al.* (2015), the authors argued that the differences in the horizontal and vertical particle accelerations are linked to the preferential sweeping mechanism of Wang & Maxey (1993). That is, a falling particle will accelerate toward the downward-moving part of an eddy, where the vertical fluid velocity changes slowly but the horizontal fluid velocity changes rapidly. While this explanation is plausible for $St \lesssim 0.3$ (where preferential sweeping is strong, as shown in § 3.2), it fails to explain the strong difference between the horizontal and vertical accelerations at higher values of St, where we observe negligible preferential sweeping for $R_\lambda \lesssim 230$. The models developed by Parishani *et al.* (2015) are for the low-St limit, whereas our approach is based on the characteristics of the Eulerian velocity field and provides a quantitative prediction for the accelerations at larger values of St.

In figure 8, we compare the DNS data for $\langle a_1^2\rangle^p$ and $\langle a_3^2\rangle^p$ to the model predictions for $St \geqslant 1$ ($Sv \geqslant 19.3$). We find that the results are in good agreement at the largest values of St, with the model being able to predict both the trends with R_λ and the decrease in the variances with increasing St. It is important to note that the trends in R_λ at high St are simply a result of the scale separation of the turbulence and are not due to intermittency effects. This is evident by the fact that our model does not account for intermittency, but can still accurately reproduce the trends with Reynolds number. At very low values of St, however, when gravity is weak (and our model no longer holds), intermittency effects are indeed important. Refer to Part 1 for a discussion of the role of intermittency on the accelerations of low-St particles.

To further explore the trends in the accelerations for particles with varying levels of inertia and gravity, we plot in figure 9 the inertial particle acceleration variances for a wide range of St and Sv at $R_\lambda = 227$. (Recall that statistics at the largest values of Sv have errors due to unphysical effects of the periodic boundary conditions. Refer to appendix A for a more detailed explanation.) As expected, the particle acceleration variances are the largest for $St \ll 1$ and $Sv \gg 1$ due to the gravitational trajectory effect, as predicted by (3.10) and (3.11). For sufficiently large St, particles filter out nearly all of the large-scale turbulence, and so acceleration variances are small. For intermediate St and Sv, the particle accelerations are determined by a combination of preferential sampling, gravitational trajectory and inertial filtering effects. We also

https://doi.org/10.1017/jfm.2016.227 Published online by Cambridge University Press

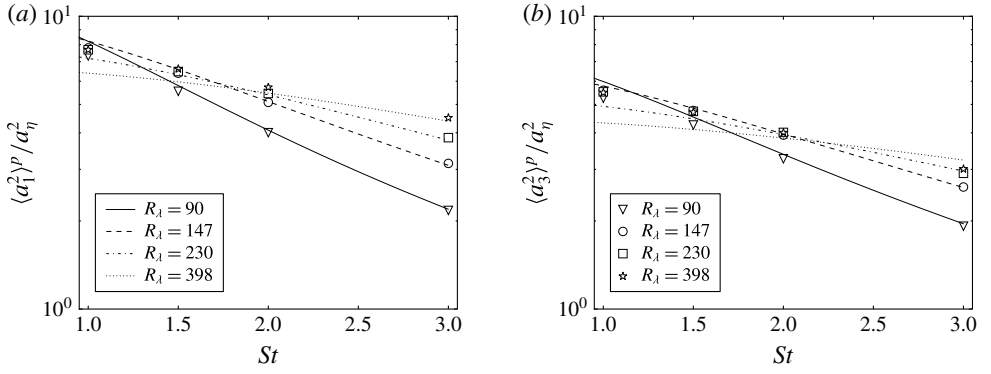

FIGURE 8. Comparison between DNS data and theoretical predictions for the variance of the particle accelerations in the horizontal (*a*) and vertical (*b*) directions at high *St*. Open symbols denote DNS data with gravity ($Fr = 0.052$), and the lines in (*a*) and (*b*) indicate the predictions from (3.10) and (3.11), respectively, for the different Reynolds numbers simulated.

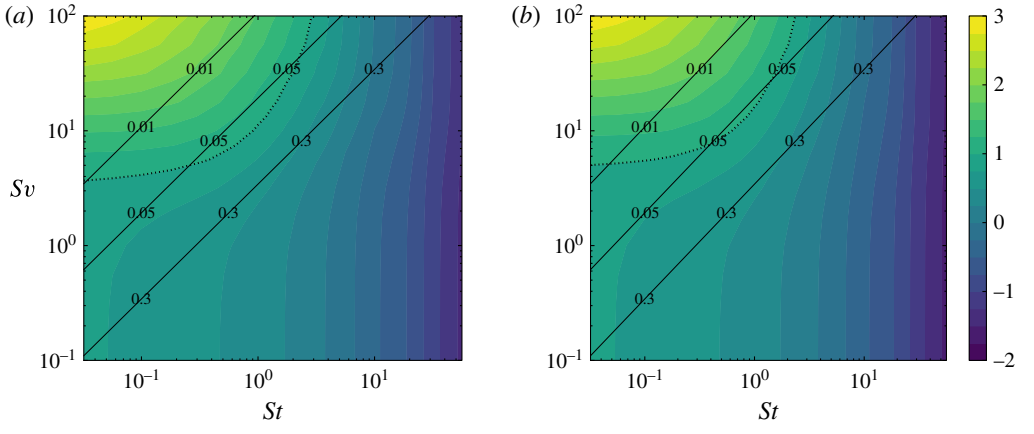

FIGURE 9. (Colour online) Filled contours of the particle acceleration variances, $\langle a_1^2\rangle^p$ (*a*) and $\langle a_3^2\rangle^p$ (*b*), normalized by the Kolmogorov acceleration variance a_η^2, for $R_\lambda = 227$. The contours are logarithmically scaled, and the labels on the colour bar denote exponents of the decade. The diagonal lines denote three different values of *Fr*, corresponding to conditions representative of stratiform clouds ($Fr = 0.01$), cumulus clouds ($Fr = 0.05$) and cumulonimbus clouds ($Fr = 0.3$). The dotted lines corresponds to $\langle a_1^2\rangle^p = a_\eta^2$ in (*a*) and $\langle a_3^2\rangle^p = a_\eta^2$ in (*b*).

observe from figure 9 that the particle acceleration variances are the largest under conditions representative of stratiform clouds ($Fr \sim 0.01$) and the smallest under conditions representative of cumulonimbus clouds ($Fr \sim 0.3$).

4. Two-particle statistics

We now consider particle-pair statistics, in particular, particle relative velocities (§ 4.1), clustering (§ 4.2) and the collision kernels (§ 4.3). In each case, we compare our results to those without gravity (from Part 1) to highlight the role of gravity.

https://doi.org/10.1017/jfm.2016.227 Published online by Cambridge University Press

4.1. *Particle relative velocities*

In this section, we examine the effect of gravity on the relative velocities of two identical inertial particles. We first discuss the expected effect of gravity on the relative velocities from a theoretical framework (§ 4.1.1), and then analyse the DNS results (§ 4.1.2).

4.1.1. *Theoretical framework for particle relative velocities*

As in Part 1, we define the relative position and velocity as $\boldsymbol{r}^p(t)$ and $\boldsymbol{w}^p(t)$, respectively, and $\boldsymbol{\Delta u}(\boldsymbol{r}^p(t), t)$ as the difference in fluid velocities at the particle locations. By subtracting (2.3) for two particles at a given instant in time, we obtain the following equation for the relative position and velocity of the two particles

$$\frac{\mathrm{d}^2\boldsymbol{r}^p}{\mathrm{d}t^2} = \frac{\mathrm{d}\boldsymbol{w}^p}{\mathrm{d}t} = \frac{\boldsymbol{\Delta u}\,(\boldsymbol{r}^p(t), t) - \boldsymbol{w}^p(t)}{\tau_p}. \tag{4.1}$$

Notice that the gravity vector precisely cancels out of this equation, making it appear as though gravity does not influence the relative motion of the particle pair; however, this is not true, as gravity has an implicit effect on the statistics of $\boldsymbol{\Delta u}(\boldsymbol{r}^p(t), t)$, and this substantially modifies the relative position and velocity statistics of the particles (as will be shown below).

Following the nomenclature in Part 1, we define the second-order particle relative velocity structure function tensor as

$$\boldsymbol{S}_2^p(\boldsymbol{r}) = \langle \boldsymbol{w}^p(t)\boldsymbol{w}^p(t)\rangle_{\boldsymbol{r}}, \tag{4.2}$$

where $\langle\cdot\rangle_{\boldsymbol{r}}$ denotes an ensemble average conditioned on $\boldsymbol{r}^p(t) = \boldsymbol{r}$. We now use the formal solution of (4.1) to construct the exact expression for $\boldsymbol{S}_2^p(\boldsymbol{r})$. This will allow us to explain the expected trends in the structure functions with inertia and gravity. The exact expression for $\boldsymbol{S}_2^p(\boldsymbol{r})$ is given by (e.g. see Pan & Padoan 2010)

$$\hat{\boldsymbol{S}}_2^p(\hat{\boldsymbol{r}}) = \frac{1}{St^2}\int_{-\infty}^{0}\int_{-\infty}^{0} \langle \boldsymbol{\Delta}\hat{\boldsymbol{u}}(\hat{\boldsymbol{r}}^p(\hat{s}), \hat{s})\boldsymbol{\Delta}\hat{\boldsymbol{u}}(\hat{\boldsymbol{r}}^p(\hat{S}), \hat{S})\rangle_{\hat{\boldsymbol{r}}}\, \exp[St^{-1}(\hat{s}+\hat{S})]\,\mathrm{d}\hat{s}\,\mathrm{d}\hat{S}, \tag{4.3}$$

where $\hat{Z}$ denotes a variable Z normalized by Kolmogorov scales.

We first consider (4.3) in the absence of gravity. From (4.3), we observe that particle relative velocities are affected by the fluid velocity difference $\boldsymbol{\Delta u}(\boldsymbol{r}^p(t), t)$ along their trajectories. For small values of St, the high damping of the exponential term in (4.3) causes contributions to the integral from the particle history to be negligible, and hence the particle relative velocities in the equation become equivalent to the instantaneous fluid velocity difference at the current particle position, reflecting the fact that preferential sampling is the dominant mechanism affecting relative particle motion. As shown in Part 1, preferential sampling causes inertial particles to experience larger fluid velocity differences than those of fluid particles in directions parallel to the particle separation vector and smaller fluid velocity differences in directions perpendicular to the particle separation vector. As St increases, in the absence of gravity, the exponential damping diminishes and the influence of the particle history becomes increasingly important. At higher St, particles retain a memory of their interactions with the turbulence, and it is the fluid velocities at larger separations along their path histories that dominate the contribution to the particle velocity dynamics, leading to particle relative velocities that are larger than

https://doi.org/10.1017/jfm.2016.227 Published online by Cambridge University Press

the local fluid velocity difference. This phenomenon has been referred to as 'caustics' (e.g. see Wilkinson & Mehlig 2005; Wilkinson *et al.* 2006). Refer to Bragg & Collins (2014*b*) for a more complete theoretical description of this phenomenon, and to Part 1 for supporting DNS evidence.

We now introduce gravity and discuss its effect on the relative velocities. Recall in § 3.1 that gravity generally reduces the degree of preferential sampling. With gravity, we therefore expect the relative velocities of small-St particles to be affected less by preferential sampling, and therefore to have dynamics closer to that of the fluid particles. At higher values of St, gravity alters the inertial particle relative velocities through its influence on the path-history mechanism. We observed in § 3.1 that gravity reduces the correlation time scales of the flow along particle trajectories. This implies that gravity causes the fluid velocity differences in (4.3) to become decorrelated more rapidly, and thus it reduces the correlation radius over which the relative velocities are influenced by their path-history interactions with the fluid. We therefore expect the particle relative velocities to be reduced by gravity. A similar explanation is given in Fouxon *et al.* (2015), where the authors also argue that path-history effects are reduced in the presence of gravity.

In addition to the magnitude changes caused by gravity, its directional nature causes the symmetry of the particle field to become anisotropic. We define the mean inward, parallel and perpendicular relative velocity statistics as

$$S^p_{-\parallel}(\boldsymbol{r}) \equiv -\int_{-\infty}^{0} w_\parallel p(w_\parallel \,|\, \boldsymbol{r})\, \mathrm{d}w_\parallel, \tag{4.4}$$

$$S^p_{2\parallel}(\boldsymbol{r}) \equiv \int_{-\infty}^{\infty} [w_\parallel]^2 p(w_\parallel \,|\, \boldsymbol{r})\, \mathrm{d}w_\parallel, \tag{4.5}$$

$$S^p_{2\perp}(\boldsymbol{r}) \equiv \int_{-\infty}^{\infty} [w_\perp]^2 p(w_\perp \,|\, \boldsymbol{r})\, \mathrm{d}w_\perp, \tag{4.6}$$

where $w_\parallel$ and $w_\perp$ are the longitudinal (i.e. parallel to the particle separation vector) and transverse (i.e. perpendicular to the particle separation vector) components of the relative velocity, respectively, and $p(w_\parallel \,|\, \boldsymbol{r})$ and $p(w_\perp \,|\, \boldsymbol{r})$ are their respective probability density functions conditioned on the separation vector $\boldsymbol{r}$. In the absence of gravity, $S^p_{2\parallel}$, $S^p_{2\perp}$, and $S^p_{-\parallel}$ are functions of the separation distance $r \equiv |\boldsymbol{r}|$ only. With gravity, these statistics become functions of the angle between the separation vector $\boldsymbol{r}$ and the gravity vector $\mathbf{g}$, here denoted as θ. A convenient way to express this dependence is to expand these functions in a spherical harmonic series

$$S^p_{-\parallel}(\boldsymbol{r}) = \sum_{\ell=0}^{\infty} C^0_{2\ell}(r) Y^0_{2\ell}(\theta), \tag{4.7}$$

$$S^p_{2\parallel}(\boldsymbol{r}) = \sum_{\ell=0}^{\infty} D^0_{2\ell}(r) Y^0_{2\ell}(\theta), \tag{4.8}$$

$$S^p_{2\perp}(\boldsymbol{r}) = \sum_{\ell=0}^{\infty} E^0_{2\ell}(r) Y^0_{2\ell}(\theta), \tag{4.9}$$

where $C^0_{2\ell}(r)$, $D^0_{2\ell}(r)$ and $E^0_{2\ell}(r)$, are the spherical harmonic coefficients, and $Y^0_{2\ell}$ are the spherical harmonic functions. In discussing the results below, we will quantify the degree of anisotropy introduced by gravity by analysing the relative magnitudes of the spherical harmonic coefficients. Similar expansions will be used to describe the anisotropic radial distribution function that results from gravity.

https://doi.org/10.1017/jfm.2016.227 Published online by Cambridge University Press

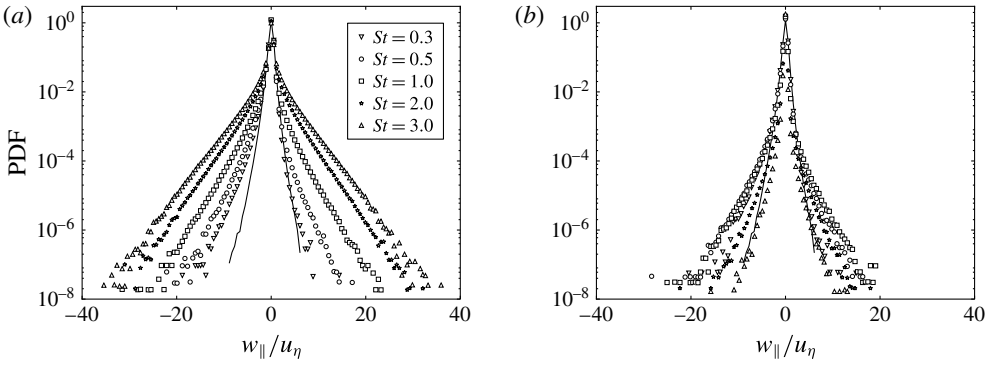

FIGURE 10. PDFs of the radial relative velocities without gravity (*a*) and with gravity ($Fr = 0.052$) (*b*) at $R_\lambda = 398$ and $0 \leqslant r/\eta \leqslant 2$. The solid line denotes data for fluid ($St = 0$) particles.

4.1.2. *Relative velocity results*

We now analyse the results from the DNS using the decompositions described in § 4.1.1. To study how gravity affects the magnitude of the relative velocity, we first consider the zeroth-order coefficients, $C_0^0(r) \equiv S^p_{-\parallel}(r)$, $D_0^0(r) \equiv S^p_{2\parallel}(r)$ and $E_0^0(r) \equiv S^p_{2\perp}(r)$, where we have taken $Y_0^0 = 1$. In effect, these coefficients represent the spherical average over the anisotropic particle field.

Figure 10 shows the probability density function (PDF) for the parallel component of the relative velocity for $0 \leqslant r/\eta \leqslant 2$, at different Stokes numbers and a fixed Reynolds number of 398. The panel on the left-hand side shows the case of no gravity and the panel on the right-hand side the case of $Fr = 0.052$. It is immediately apparent that gravity has a profound effect on the PDFs, causing a dramatic reduction in the tails of the distribution, particularly for particles with larger Stokes numbers. This is consistent with the explanation given in § 4.1.1, which argued that gravity suppresses path-history effects, thereby reducing the relative velocities.

We next consider the relative velocity variances as a function of the separation distance. Figure 11 shows the spherically averaged quantities $S^p_{2\parallel}(r)$ and $S^p_{2\perp}(r)$. For $St \geqslant 1$ (corresponding to $Sv \geqslant 19.3$), we observe that gravity strongly decreases the relative velocities, by orders of magnitude in some cases. The explanation is that gravity reduces the effect of the path-history interactions, causing a reduction in the relative velocities (cf. § 4.1.1).

Data at $St = 0.3$ are shown in the insets in figure 11. For $St = 0.3$ and very small separations ($r/\eta \lesssim 1$), the relative velocities show evidence of path-history effects (see also Part 1), causing the relative velocities to exceed those of $St = 0$ particles in both the parallel and perpendicular directions. However, at larger separations ($1 \lesssim r/\eta \lesssim 10$), the perpendicular relative velocities become less than those of $St = 0$ particles, as expected, as a result of preferential sampling. We also see that gravity causes the relative velocities to approach those of the underlying fluid, since it decreases preferential sampling effects. These trends are consistent with the discussion in § 4.1.1. (Note that since particles with $St < 0.3$ have only weak gravitational forces ($Sv < 5.79$), the effect of gravity on the relative velocities is less apparent and data from these particle classes are therefore not shown.)

https://doi.org/10.1017/jfm.2016.227 Published online by Cambridge University Press

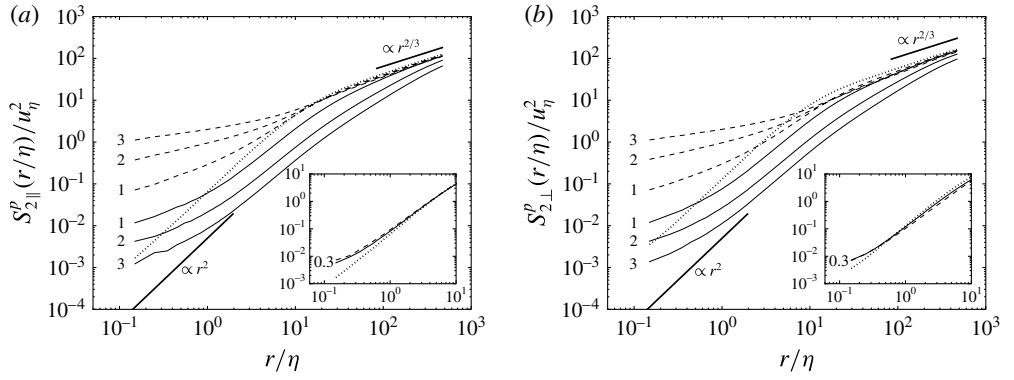

FIGURE 11. The variance of the particle relative velocities parallel to the separation vector (*a*) and perpendicular to the separation vector (*b*) for $R_\lambda = 398$, plotted as a function of r/η for different St. The thin solid lines indicate data with gravity ($Fr = 0.052$), the dashed lines indicate data without gravity, and the thick dotted line indicates fluid ($St = 0$) particles. The Stokes numbers are indicated by the line labels, and the fluid velocity scalings are indicated by thick solid lines. The main plots show $St = 0$ and $St \geqslant 1$, while the insets show $St = 0$ and $St = 0.3$.

The decreased influence of path-history interactions is also apparent in the scaling of the relative velocity variances in figure 11. In the dissipation range, the fluid relative velocity variances are proportional to r^2. In the absence of gravity, the relative velocities for $St \geqslant 1$ do not exhibit r^2-scaling over any portion of the dissipation range, as was noted in Part 1. However, with gravity, we see a clearer r^2-scaling extending much deeper into the dissipation range for $1 \lesssim r/\eta \lesssim 10$. Compared to the case without gravity, one has to go to smaller separations to observe deviations from r^2 scaling, as gravity reduces the path-history effect responsible for the formation of caustics.

Of particular interest to the collision kernel is the mean inward velocity (cf. § 4.3). In general, the mean inward velocity is more difficult to analyse theoretically than the relative velocity variance, but qualitatively we expect both statistics to follow the same trends. In figure 12, we show $S^p_{-\parallel}$ at $R_\lambda = 398$, both with and without gravity. We see that the mean inward velocities, like the variances, decrease with the addition of gravity at large St due to the reduced influence of the path-history mechanism and at small St due to the reduced influence of the preferential sampling mechanism. Interestingly, with gravity, the mean inward relative velocities (in contrast to the relative velocity variances) follow the local fluid scaling almost perfectly throughout the entire dissipation range. This result was also noted in Bec *et al.* (2014). One plausible explanation is that since the mean inward velocity is a lower-order statistic than the velocity variance, it is less affected by path-history interactions and is more affected by the local fluid turbulence, causing the scaling exponents to increase (see Part 1).

To further verify our arguments in § 4.1.1, it is helpful to decouple the effects of gravity and inertia by varying each independently. We do so in figure 13, where we show $S^p_{-\parallel}$ and $S^p_{2\parallel}$ for various St and Sv. While the results at high Sv are likely artificially affected by the periodic boundary conditions (see appendix A), we can still use these data to discuss the qualitative trends in the relative velocities at different values of St and Sv. We see that $S^p_{-\parallel}$ and $S^p_{2\parallel}$ have similar qualitative trends. For

https://doi.org/10.1017/jfm.2016.227 Published online by Cambridge University Press

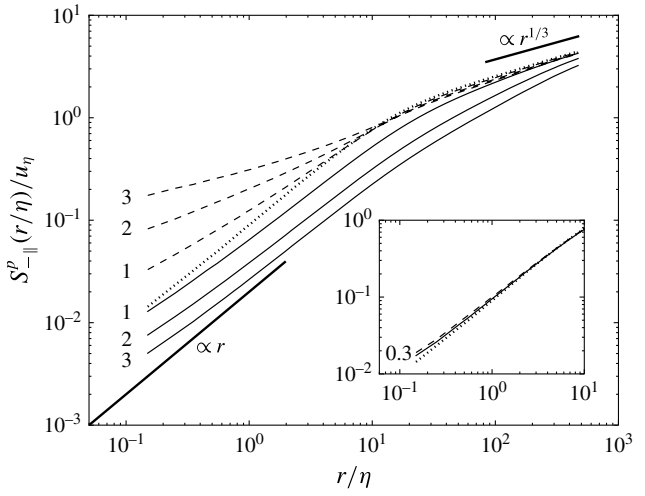

FIGURE 12. The mean inward particle relative velocity for $R_\lambda = 398$, plotted as a function of r/η for different St. The thin solid lines indicate data with gravity ($Fr = 0.052$), the dashed lines indicate data without gravity and the thick dotted line indicates fluid ($St = 0$) particles. The Stokes numbers are indicated by the line labels and the fluid velocity scalings are shown by thick solid lines. The main plot shows $St = 0$ and $St \geqslant 1$, while the inset shows $St = 0$ and $St = 0.3$.

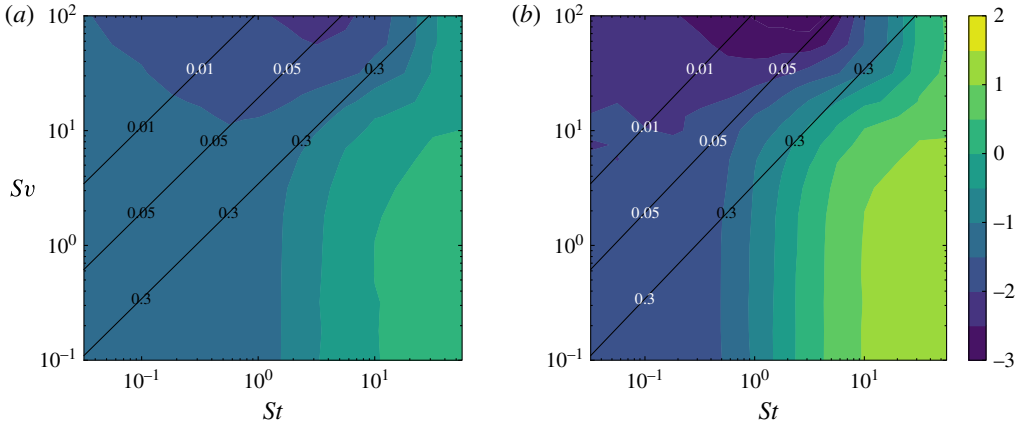

FIGURE 13. (Colour online) Filled contours of $S^p_{-\parallel}(r/\eta)/u_\eta$ (*a*) and $S^p_{2\parallel}(r/\eta)/u^2_\eta$ (*b*) evaluated at $r/\eta = 0.25$ and $R_\lambda = 227$ for different values of St and Sv. The contours are logarithmically scaled, and the colour bar labels indicate the exponents of the decade. The diagonal lines denote three different values of Fr, corresponding to conditions representative of stratiform clouds ($Fr = 0.01$), cumulus clouds ($Fr = 0.05$) and cumulonimbus clouds ($Fr = 0.3$).

$Sv \lesssim 10$, both quantities increase with increasing St, either due to preferential sampling effects (at low St) or path-history effects (at high St). The relative velocities also decrease with increasing Sv, since gravity causes both effects to be less significant, as discussed in § 4.1.1. Finally, we observe that the relative velocities are the smallest

https://doi.org/10.1017/jfm.2016.227 Published online by Cambridge University Press

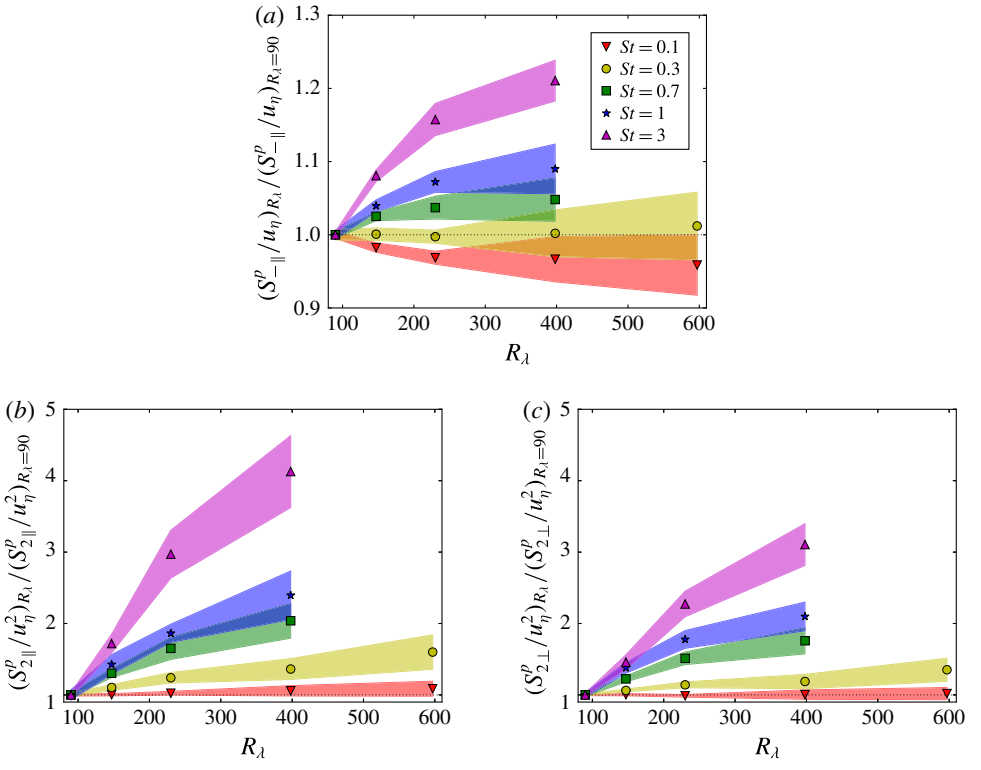

FIGURE 14. (Colour online) (*a*) $S^p_{-\parallel}/u_\eta$, (*b*) $S^p_{2\parallel}/u^2_\eta$ and (*c*) $S^p_{2\perp}/u^2_\eta$, plotted as a function of R_λ for various St. The relative velocities are shown at $r/\eta = 0.25$ and the quantities at a given Reynolds number are divided by their corresponding value at $R_\lambda = 90$. Shaded contours denote 95 % confidence intervals. Note that (*a*) has a much smaller ordinate scale than (*b*) and (*c*).

for the largest values of Sv and $St \sim 1$. At smaller St, preferential concentration effects are more significant, while at larger St, path-history effects are more significant. Both effects lead to an increase in the relative velocities. An implication of these results for clouds is that for a given value of St, droplets in stratiform clouds ($Fr = 0.01$) will generally have smaller relative velocities than droplets in cumulonimbus clouds ($Fr = 0.3$).

We have thus far examined and explained relative velocity statistics for fixed Reynolds numbers. We now consider how these statistics are affected by changes in R_λ. In figure 14, we show $S^p_{-\parallel}/u_\eta$, $S^p_{2\parallel}/u^2_\eta$ and $S^p_{2\perp}/u^2_\eta$. In Part 1, we noted that $S^p_{2\parallel}/u^2_\eta$ increases weakly with increasing R_λ in the absence of gravity for $0.3 \lesssim St \lesssim 1$, and attributed this trend to the increased scale separation with increasing R_λ, which causes a few inertial particles to be affected by their memory of increasingly energetic turbulence. (We also suggested that increased intermittency effects at higher Reynolds numbers could contribute to the observed trends.) While we expected the increased scale separation of the turbulence to also increase the relative velocities for higher-St particles, we instead found that the relative velocities decreased with increasing R_λ for $1 \lesssim St \lesssim 3$. We argued that this trend was caused by a corresponding decrease in the rotation time scales T^p_{RR}/τ_η, which in turn reduced the influence of path-history

https://doi.org/10.1017/jfm.2016.227 Published online by Cambridge University Press

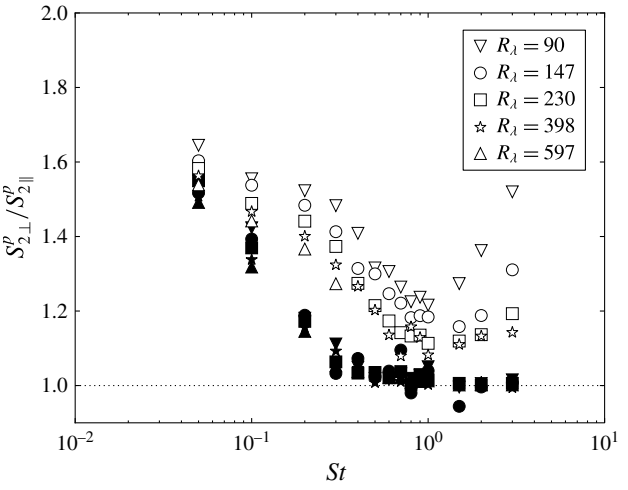

FIGURE 15. $S^p_{2\perp}/S^p_{2\parallel}$, evaluated at $r/\eta = 0.25$, and plotted as a function of St for different values of R_λ. Open symbols denote the case with gravity ($Fr = 0.052$) and the filled symbols denote the case without gravity.

effects and decreased the relative velocities. However, with gravity, we find that T^p_{RR}/τ_η is generally independent of R_λ (see § 3.1), and thus we expect that this allows the increased scale separation of the turbulence to cause $S^p_{2\parallel}/u^2_\eta$ to uniformly increase with increasing R_λ for $St \gtrsim 0.3$. Our results in figure 14(*b*) confirm this expectation. We also see that $S^p_{-\parallel}/u_\eta$ is generally unaffected by changes in R_λ (figure 14*a*), since it is less influenced by the relatively infrequent occurrences of the effects discussed above. We are also interested in the effect of the Reynolds number on the perpendicular relative velocities, since these statistics will also affect the degree of particle clustering (see § 4.2). From figure 14(*c*), we see that the trends with R_λ in the perpendicular direction are identical to those in the parallel direction.

In Part 1, we found that without gravity, the parallel and perpendicular relative velocities became equivalent at small separations for $St \gtrsim 0.3$. The physical explanation is that the path-history contribution to their relative velocities decreases the coherence of the pair motion, and in the ballistic limit where the pairs move independently of each other, the parallel and perpendicular components are equal. However, with gravity, path-history effects are weaker, and thus the parallel and perpendicular velocities may not be the same in this regime.

We compare these two quantities in figure 15 by plotting $S^p_{2\perp}/S^p_{2\parallel}$ at $r/\eta = 0.25$. We see that both with and without gravity, the ratio $S^p_{2\perp}/S^p_{2\parallel}$ approaches 2 at low Stokes numbers, the value for fluid particles (e.g. see Pope 2000). For $St \gtrsim 0.3$ without gravity, $S^p_{2\perp}$ and $S^p_{2\parallel}$ are equivalent, as expected. At high values of St with gravity, however, the parallel and perpendicular components are not equivalent, since path-history effects are weakened by gravity. As R_λ increases, the particle relative velocities are affected by increasingly energetic turbulence along their path histories. As a result, the relative velocities are larger and the particles move more ballistically, causing the ratio $S^p_{2\perp}/S^p_{2\parallel}$ to decrease with increasing R_λ.

We now examine the effects of Reynolds number on the scaling of the relative velocities. As in Part 1, we compute the scaling exponents of the mean inward relative velocity ($\zeta^-_\parallel$) and the relative velocity variance ($\zeta^2_\parallel$) by performing linear least-squares

https://doi.org/10.1017/jfm.2016.227 Published online by Cambridge University Press

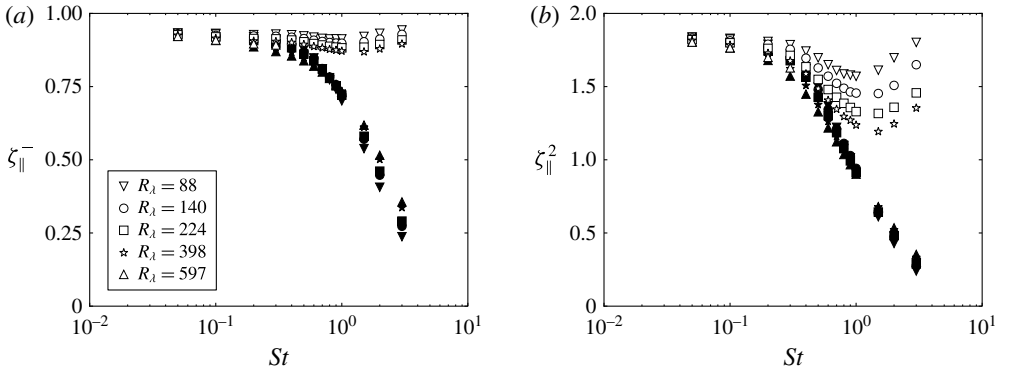

FIGURE 16. The scaling exponents of the mean inward relative velocities (*a*) and relative velocity variances (*b*) plotted as a function of St for different values of R_λ. The open symbols denote the case with gravity ($Fr = 0.052$) and the filled symbols denote the case without gravity. The scaling exponents are computed using linear least-squares regression over the range $0.75 \leqslant r/\eta \leqslant 2.75$.

power-law fits over separations $0.75 \leqslant r/\eta \leqslant 2.75$. While the results in figure 11 suggest that the power-law exponent may vary considerably over this range, we are forced to use this relatively large range to gather sufficient statistics at the smaller separations. Thus, while these scaling exponents allow us to assess the trends with R_λ, they only provide a qualitative understanding, as the scaling varies considerably throughout the dissipation range and this variation is not completely captured by this analysis.

The scaling exponents are shown in figure 16. The trends at a given value of R_λ are in agreement with our observations from figures 11 and 12, which are explained above. We also see that with gravity, the scaling exponents tend to decrease with increasing R_λ, since the particles are more influenced by their memory of increasingly energetic turbulence and therefore tend to move ballistically, as noted above.

Angular distributions of $S^p_{-\parallel}(\boldsymbol{r})/S^p_{-\parallel}(r)$ are presented in figure 17 for a range of Stokes numbers, $R_\lambda = 398$, and $r < \eta$. The anisotropy of the distribution is reflected in the colour variation over the surface of the sphere. We see immediately that the asymmetry in the relative velocities follows opposite trends at small and large St. That is, at small St, the relative velocities are largest for particles separated in the vertical direction, whereas for $St \gtrsim 1$, the opposite is true. The explanation is as follows. At small separations and $St \lesssim 0.3$, particle pairs that are separated vertically will have parallel relative velocities that are proportional to $S_{33}(\boldsymbol{x}^p(t), t)$, the longitudinal velocity gradient in the vertical direction as sampled by inertial particles (see § 3.1). Particle pairs that are separated along the horizontal direction, however, will have parallel relative velocities that are proportional to $S_{11}(\boldsymbol{x}^p(t), t)$, the longitudinal velocity gradient in the horizontal direction. In § 3.1, we observed that particles tend to preferentially sample flow where the vertical velocity gradients are larger and the horizontal velocity gradients are smaller. As a result, the relative velocities are expected to be larger for particles that are separated in the vertical direction and smaller for particles that are separated in the horizontal directions. At large St, however, the relative velocities are smallest for particles that are separated vertically. The physical explanation is that the correlation time scales of the fluid velocity

https://doi.org/10.1017/jfm.2016.227 Published online by Cambridge University Press

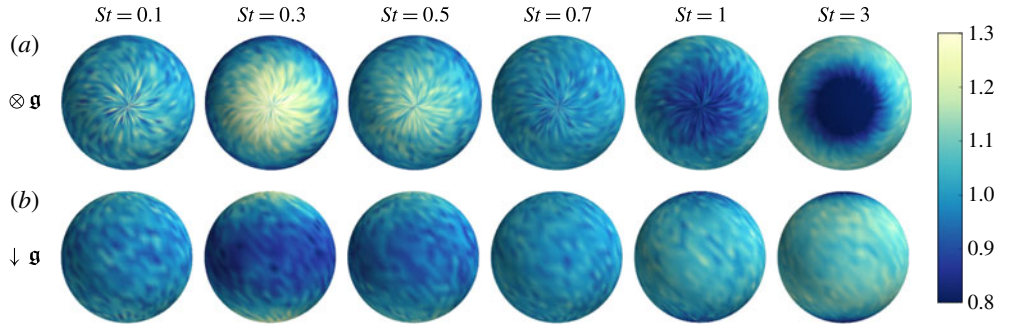

FIGURE 17. (Colour online) The directionally dependent mean inward relative velocity $S^p_{-\parallel}(\boldsymbol{r})$, normalized by the spherically averaged mean inward relative velocity $S^p_{-\parallel}(r)$, shown on a unit sphere for $R_\lambda = 398$ and $r < \eta$ with gravity ($Fr = 0.052$). The different columns correspond to different values of St. (*a*) Shows the projection where gravity is directed into the page and (*b*) shows the projection where gravity is directed downward.

gradients along this direction are the smallest (see § 3.1) and thus the particles have a weaker response to vertical fluid velocity fluctuations and correspondingly lower particle relative velocities along this direction.

Next, we consider the dependence of the anisotropy on the separation distance by plotting the spherical harmonic coefficients of order 2 and 4 as a function of r in figure 18. (Coefficients above order 4 are too small to measure accurately and thus are not shown.) We see that the anisotropy in the relative velocities generally decreases with increasing separation. The physical explanation is that with increasing separation distance, the particle motions are increasingly dependent on larger eddies, and the relative velocities induced by these isotropic eddies are increasingly energetic relative to the anisotropic velocities induced by gravity.

For small values of St, C_2^0 and C_4^0 are positive, indicating that the particle relative velocities are strongest for particles that are separated vertically. The opposite is true at large St. These observations are in agreement with the trends shown in figure 17. We also see that C_2^0 and C_4^0 tend to become more isotropic at high St and less isotropic at low St as R_λ increases. While the physical explanation for the trend at low St is unclear, at high St, we expect that this increase in isotropy is linked to the increase in the relative velocities with increasing R_λ. That is, as the overall relative velocities increase, the anisotropic velocities induced by gravity will be comparatively weaker, and thus the particle relative velocities will be more isotropic.

4.2. *Particle clustering*

In this section, we consider how gravity affects the inertial particle clustering process. We first provide a theoretical explanation for the clustering (§ 4.2.1) and then compare the predictions to DNS results (§ 4.2.2).

4.2.1. *Theoretical framework for particle clustering*

We use the angular distribution function $g(\boldsymbol{r})$ (hereafter 'ADF,' see Gualtieri, Picano & Casciola 2009) to quantify the degree and orientation of particle clustering. We define $g(\boldsymbol{r})$ as

$$g(\boldsymbol{r}) \equiv \frac{N(r,\theta,\phi)/V(r,\theta,\phi)}{N/V}. \tag{4.10}$$

https://doi.org/10.1017/jfm.2016.227 Published online by Cambridge University Press

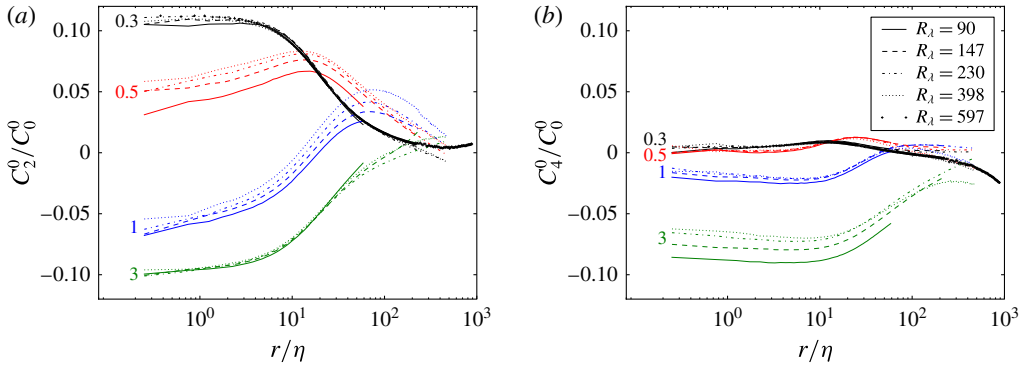

FIGURE 18. (Colour online) The second (a) and fourth (b) spherical harmonic coefficients of $S^p_{-\parallel}(\boldsymbol{r})$, normalized by the zeroth spherical harmonic coefficient, plotted as a function of r/η for different St and R_λ with gravity ($Fr = 0.052$). The different values of St considered (0.3, 0.5, 1, 3) are shown in black, red, blue and green, respectively, and the Stokes numbers are indicated by the line labels.

In this equation, $N(r, \theta, \phi)$ denotes the number of particle pairs in a truncated spherical cone with nominal radius r, polar angle θ and azimuthal angle ϕ. The volume of the truncated spherical cone $V(r, \theta, \phi)$ is given by

$$V(r, \theta, \phi) \equiv \sin(\theta)\Delta\theta\Delta\phi[(r + \Delta r)^3 - (r - \Delta r)^3]/3, \tag{4.11}$$

where Δr is the radial width, $\Delta\theta$ is the extent of the polar angle and $\Delta\phi$ is the extent of the azimuthal angle.

As discussed in § 4.1.1, the equation governing the relative motion of like particles, (4.1) is the same with and without gravity. Hence the theory of Zaichik & Alipchenkov (2009), developed without consideration of gravitational settling, is not explicitly changed by the presence of gravity; instead gravity modifies the equation through implicit changes to its coefficients. From Zaichik & Alipchenkov (2009) (see also Bragg & Collins 2014*a*), the equation describing $g(\boldsymbol{r})$ at steady state is

$$\boldsymbol{0} = -St\tau_\eta\left(\boldsymbol{S}_2^p + \boldsymbol{\lambda}\right) \cdot \boldsymbol{\nabla}_{\boldsymbol{r}} g - St\tau_\eta g \boldsymbol{\nabla}_{\boldsymbol{r}} \cdot \boldsymbol{S}_2^p, \tag{4.12}$$

where $\boldsymbol{\lambda}$ is the dispersion tensor describing the influence of the fluid velocity difference field on the dispersion of the particles (see Bragg & Collins 2014*a*).

Since $\boldsymbol{S}_2^p$ is anisotropic with gravity (cf. § 4.1.2), so too is the ADF $g(\boldsymbol{r})$, as is evident in (4.12). We similarly adopt an expansion of the ADF in terms of spherical harmonic functions

$$g(\boldsymbol{r}) = \sum_{\ell=0}^{\infty} \mathscr{C}_{2\ell}^0(r) Y_{2\ell}^0(\theta), \tag{4.13}$$

where $\mathscr{C}_{2\ell}^0$ are the spherical harmonic coefficients for the ADF. We only attempt to model the zeroth-order term, which we denote as

$$g(r) = \mathscr{C}_0^0(r). \tag{4.14}$$

where $Y_0^0 \equiv 1$. Note that $g(r)$ is just the spherical average of the ADF $g(\boldsymbol{r})$, or the equivalent of the radial distribution function (RDF) defined in Part 1. While this

https://doi.org/10.1017/jfm.2016.227 Published online by Cambridge University Press

approach captures the leading-order contribution of gravity to the ADF, it does not predict the gravity-induced anisotropy. (Note that a similar approach was adopted by Alipchenkov & Beketov (2013) to model particle clustering in a homogeneous turbulent shear flow.) We will assess the accuracy of this approach in § 4.2.2.

We therefore consider the isotropic form of (4.12), which is given as

$$0 = \underbrace{-St\left(\hat{S}^p_{2\parallel} + \hat{\lambda}_\parallel\right)}_{\equiv\mathfrak{D}} \nabla_{\hat{r}} g \underbrace{-St\left(\nabla_{\hat{r}}\hat{S}^p_{2\parallel} + 2\hat{r}^{-1}\left[\hat{S}^p_{2\parallel} - \hat{S}^p_{2\perp}\right]\right)}_{\equiv\mathfrak{d}} g, \tag{4.15}$$

where $\hat{Z}$ denotes a variable Z normalized by Kolmogorov scales. $\lambda_\parallel$ denotes the projection of the dispersion tensor $\boldsymbol{\lambda}$ along a direction parallel to the particle separation vector. We note that the first term on the right-hand side is associated with outward diffusion (which acts to reduce the RDF), while the second is associated with an inward drift (which acts to increase the RDF). The corresponding diffusion and drift coefficients are denoted as $\mathfrak{D}$ and $\mathfrak{d}$, respectively (see Bragg & Collins 2014*a*).

As explained in Bragg & Collins (2014*a*), the overall degree of clustering is determined by the relative strength of the drift and diffusion coefficients, $\mathfrak{d}/\mathfrak{D}$. Increases (decreases) in this ratio are associated with increased (decreased) clustering. To understand how gravity affects the clustering, we therefore need to understand its effect upon the ratio $\mathfrak{d}/\mathfrak{D}$.

Bragg & Collins (2014*a*) demonstrated that in the limit $St \ll 1$, $\mathfrak{D}$ and $\mathfrak{d}$ simplify to

$$\mathfrak{D} \approx -\hat{r}^2 B_{nl}, \tag{4.16}$$

and

$$\mathfrak{d} \approx -St\hat{r}(\langle\hat{S}^2\rangle^p - \langle\hat{R}^2\rangle^p)/3, \tag{4.17}$$

respectively, where B_{nl} is the non-local coefficient defined in Chun *et al.* (2005) that is independent of the particle Stokes number. As is evident in (4.16), the diffusion term is independent of the Stokes number – hence $\mathfrak{D}$ is unaffected by gravity in this limit. In contrast, $\mathfrak{d}$ is proportional to both St and $\langle\hat{S}^2\rangle^p - \langle\hat{R}^2\rangle^p$. Gravity reduces the correlation between the particles and the strain and rotation fields, and thereby reduces $\mathfrak{d}$. The net effect of gravity in this limit is therefore to reduce the ratio $\mathfrak{d}/\mathfrak{D}$ and the degree of clustering. We also note that at low St, the trends in the strain and rotation rates with R_λ are very weak. Consistent with Part 1, these trends imply the clustering to be nearly independent of R_λ in the limit $St \ll 1$, with or without gravity.

For inertial particles with intermediate Stokes numbers in the range $0.2 \lesssim St \lesssim 0.7$ (note that this range is approximate and is likely sensitive to changes in Reynolds number, as mentioned in Part 1), we no longer have simple relationships for the drift and diffusion terms. However, we can still make qualitative predictions for the trends in the clustering based on our physical understanding and the explanations in Bragg & Collins (2014*a*). Over this range of St, Bragg & Collins (2014*a*) argued that both preferential sampling effects and path-history effects act to increase clustering, with the path-history effects becoming increasingly dominant as St increases. Since gravity decreases both preferential sampling and path-history effects, we therefore expect it to reduce clustering over the approximate range of $0.2 \lesssim St \lesssim 0.7$.

We next use (4.15) to understand clustering at larger values of St. In Part 1, we argued that without gravity, $\hat{S}^p_{2\parallel} \approx \hat{S}^p_{2\perp}$ for $St \gtrsim 0.3$, and we were thus able to neglect

https://doi.org/10.1017/jfm.2016.227 Published online by Cambridge University Press

the term $2\hat{r}^{-1}(\hat{S}^p_{2\parallel} - \hat{S}^p_{2\perp})$ in (4.15) at high St. However, with gravity, the parallel and perpendicular relative velocity variances are generally not equal (as discussed in § 4.1.2), and hence this term must be retained. We are still able to neglect $\hat{\lambda}_\parallel$ at small separations and high St, since this term is inversely proportional to St and decreases as the time scales of the fluid velocity seen by the particles decrease (see Bragg & Collins 2014*a*).

The simplified form of (4.15) at high St is therefore

$$0 = \underbrace{-St\hat{S}^p_{2\parallel}}_{\mathfrak{D}} \nabla_{\hat{r}} g \underbrace{-St\left(\nabla_{\hat{r}}\hat{S}^p_{2\parallel} + 2\hat{r}^{-1}\left[\hat{S}^p_{2\parallel} - \hat{S}^p_{2\perp}\right]\right)}_{\mathfrak{d}} g. \tag{4.18}$$

Taking the ratio between the drift and diffusion coefficients gives us

$$\frac{\mathfrak{d}}{\mathfrak{D}} = \frac{\nabla_{\hat{r}}\hat{S}^p_{2\parallel} + 2\hat{r}^{-1}\left[\hat{S}^p_{2\parallel} - \hat{S}^p_{2\perp}\right]}{\hat{S}^p_{2\parallel}} = \frac{1}{\hat{r}}\left(\zeta^2_\parallel + 2 - 2\hat{S}^p_{2\perp}/\hat{S}^p_{2\parallel}\right), \tag{4.19}$$

where $\zeta^2_\parallel$ is the scaling exponent of the parallel relative velocity variance (see § 4.1.2).

From § 4.1.2, we see that with gravity, $\zeta^2_\parallel$ increases very strongly, while $2\hat{S}^p_{2\perp}/\hat{S}^p_{2\parallel}$ increases weakly. We expect that $\zeta^2_\parallel - 2\hat{S}^p_{2\perp}/\hat{S}^p_{2\parallel}$ will therefore increase with gravity, leading to an increase in the clustering at high St. We attribute these trends to the fact that gravity reduces the influence of path-history effects on particle relative motion in the dissipation range at high St. Path-history effects primarily act to diminish clustering for $St \gtrsim 1$ (see Bragg & Collins 2014*a*), and thus gravity reduces their influence and therefore acts to increase $g(\hat{r})$. We emphasize that this does not necessarily imply that gravity increases the inward drift and decreases the outward diffusion. In fact, our data indicate that gravity decreases both $\mathfrak{d}$ and $\mathfrak{D}$. The reduction in $\mathfrak{D}$ with gravity, however, is stronger than the corresponding reduction in $\mathfrak{d}$, causing the ratio $\mathfrak{d}/\mathfrak{D}$, and therefore the clustering strength, to increase. We also see from § 4.1.2 that increasing R_λ, with gravity, generally leads to a decrease in both $\zeta^2_\parallel$ and $\hat{S}^p_{2\perp}/\hat{S}^p_{2\parallel}$, due to the increased influence of path-history effects on particle relative motion at higher Reynolds numbers. While both quantities seem to be decreased by about the same amount with increasing R_λ, the latter quantity has a greater effect on the clustering since it is multiplied by a factor of two in (4.19). This explains why $\mathfrak{d}/\mathfrak{D}$ decreases as R_λ increases, leading to a decrease in the clustering.

In summary, gravity reduces clustering at low and intermediate values of St, but increases clustering at high values of St. Gravity reduces both preferential sampling and path-history effects. Preferential sampling effects increase clustering at low values of St, and thus gravity reduces clustering by weakening the preferential sampling drift mechanism. At intermediate values of St, both preferential sampling and path-history effects act to increase clustering, and thus gravity, by weakening both effects, reduces clustering. At higher values of St, path-history effects act to diminish clustering, and gravity increases clustering by decreasing path-history effects.

This explanation is consistent with arguments put forth by Franklin *et al.* (2007), Ayala *et al.* (2008), Onishi *et al.* (2009), Woittiez *et al.* (2009), Rosa *et al.* (2013) for low-Stokes-number particles. However, at higher Stokes numbers, several of these authors argued that gravity facilitates interactions with large-scale turbulent eddies, which in turn leads to increased particle clustering (Franklin *et al.* 2007;

https://doi.org/10.1017/jfm.2016.227 Published online by Cambridge University Press

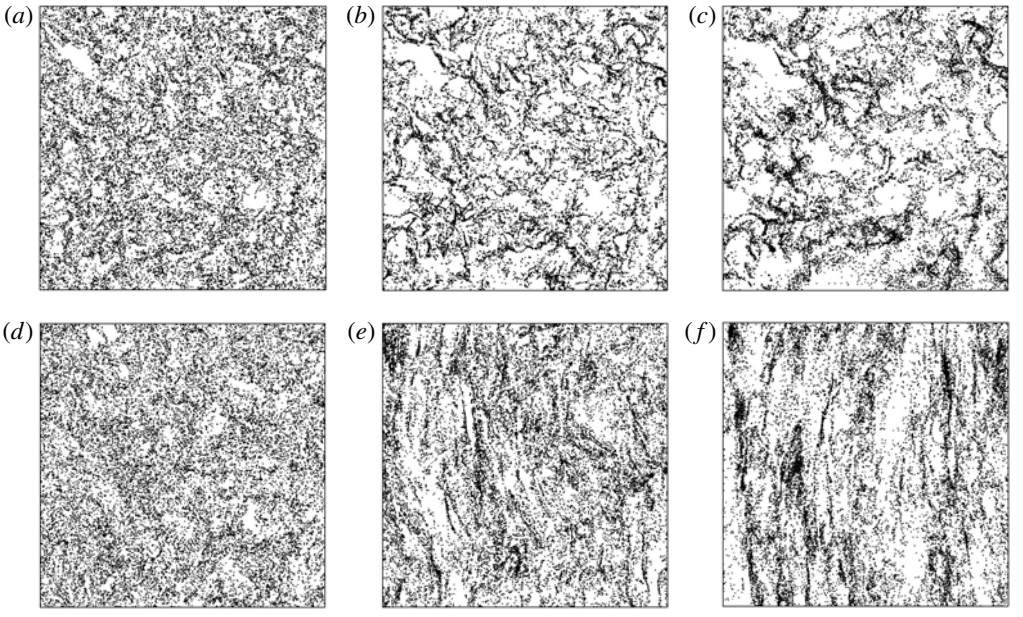

FIGURE 19. Instantaneous particle locations in $1000\eta \times 1000\eta \times 10\eta$ slices of the domain for different values of St (0.3 (*a*,*d*), 1 (*b*,*e*), 3 (*c*,*f*)) and $R_\lambda = 398$. Panels (*a–c*) are for the case without gravity, and (*d–f*) are for the case with gravity ($Fr = 0.052$), with the gravitational vector pointing downward.

Woittiez *et al.* 2009; Rosa *et al.* 2013), an hypothesis stated without supporting data, theory or a physical argument. In contrast, we argue that gravity reduces the temporal correlation radius over which the particles are affected by their path-history interactions with the turbulence, and therefore causes the particle relative motion in the dissipation range to be less affected by their interaction with larger-scale turbulence. Our hypothesis is supported by our DNS results for the relative velocities (§ 4.1.2) and also by the extension of the theoretical model of Zaichik & Alipchenkov (2009) shown above. We will show in § 4.2.2 that this model is able to reproduce the DNS clustering results very well.

Another recent paper by Park & Lee (2014) suggests the increase in particle clustering with gravity at high Stokes numbers is linked to the skewness of the vertical velocity gradients of the underlying fluid. This proposed explanation, however, seems to be flawed, and we suggest that their finding reflects a certain correlation in the system, but not a causal relation. This conclusion is supported by the recent work of Gustavsson *et al.* (2014), who observed qualitatively similarly strong clustering of high-Stokes-number particles in the presence of gravity in their random Gaussian flow field, whose fluid velocity, by definition, has no skewness.

4.2.2. *Particle clustering results*

We begin by first examining instantaneous snapshots of particle positions in the simulations in figure 19. From these visualizations, it is evident that gravity alters both the degree and orientation of the clusters and generally causes them to be aligned with the gravity vector. Recall that the clustering observed at $St \gtrsim 1$ is not related to the Maxey centrifuge mechanism (Maxey 1987), but rather is due to the history effect

https://doi.org/10.1017/jfm.2016.227 Published online by Cambridge University Press

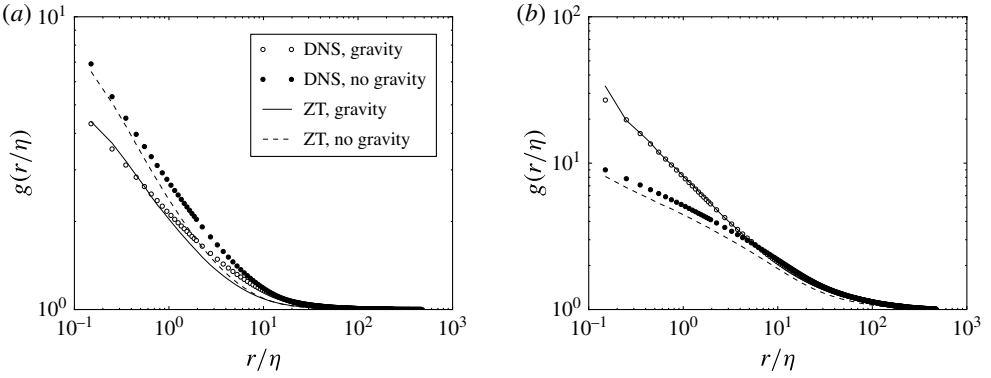

FIGURE 20. DNS (symbols) and theoretical ('ZT', lines) data for the RDFs g plotted as a function of r/η at $R_\lambda = 398$ both with gravity (open symbols and solid lines) and without gravity (filled symbols and dashed lines). (a) Shows RDFs for $St = 0.3$, and (b) for $St = 3$. The theoretical predictions are calculated from the equations in Zaichik & Alipchenkov (2009) with the non-local correction from Bragg & Collins (2014*a*), using our DNS data to specify T^p_{SS}, $S^p_{2\parallel}$ and $S^p_{2\perp}$.

(Bragg & Collins 2014*a*; Bragg, Ireland & Collins 2015*a*,*b*). This explains why higher-Stokes-number particles show signs of clustering even though they nearly uniformly sample the strain and rotation fields (cf. figure 2).

To quantify the clustering, we first consider the spherically averaged RDFs $g(r)$ to analyse the overall effect of gravity on the degree of clustering. Figure 20 shows plots of the RDFs both with gravity ($Fr = 0.052$) and without gravity. The results show gravity causes the RDFs to decrease at low St and to increase at high St, in agreement with our arguments in § 4.2.1 and earlier findings (Franklin *et al.* 2007; Ayala *et al.* 2008; Onishi *et al.* 2009; Woittiez *et al.* 2009; Rosa *et al.* 2013; Bec *et al.* 2014; Gustavsson *et al.* 2014). For sufficiently large separations, the RDFs with and without gravity approach each other.

To test the theory in § 4.2.1, we compute $g(r)$ from (4.15) using the relative velocity statistics $S^p_{2\parallel}$ and $S^p_{2\perp}$ obtained from DNS. In addition, we use the directionally averaged strain time scales T^p_{SS} from the DNS (see § 3.1) and the non-local closure proposed in Bragg & Collins (2014*a*) to compute the dispersion tensor. This allows us to test the formulation of (4.15) and the theoretical arguments in § 4.2.1. Figure 20 shows that the theory captures the quantitative results in the DNS well, indicating that (4.15) is an accurate model even for an anisotropic particle phase, and thus verifies the physical explanations presented in § 4.2.1.

Next, we consider the dependence of the RDFs on R_λ in figure 21. As was the case without gravity (see Part 1), the RDFs are largely independent of R_λ for $St \lesssim 1$ with gravity. This is in agreement with our arguments in § 4.2.1 and implies that small-St clustering is a small-scale phenomenon (both with and without gravity) that is generally unaffected by the intermittency of the turbulence. For $St > 1$ the RDFs generally increase with increasing R_λ, since the ratio between the drift and diffusion increases, as discussed in § 4.2.1. The RDFs seem to approach a constant value, however, suggesting that any Reynolds-number dependencies may eventually saturate in the limit $R_\lambda \to \infty$.

https://doi.org/10.1017/jfm.2016.227 Published online by Cambridge University Press

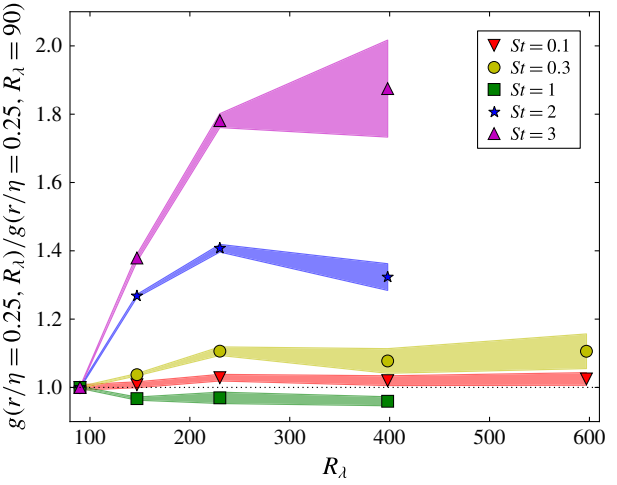

FIGURE 21. (Colour online) The normalized RDFs at $r/\eta = 0.25$ with gravity ($Fr = 0.052$), plotted as a function of R_λ. The RDFs at a given Reynolds number are normalized by their corresponding value at $R_\lambda = 90$ to highlight the Reynolds-number dependence. Shaded contours denote 95 % confidence intervals for the RDFs.

We can also quantify the degree of small-scale clustering by performing a power-law fit of the RDFs (Reade & Collins 2000) at small separations,

$$g(r) \approx c_0 \left(\frac{\eta}{r}\right)^{c_1}, \tag{4.20}$$

as discussed in Part 1. The power-law fits are performed over the range $0.75 \leqslant r/\eta \leqslant 2.75$, and the calculated values of c_0 and c_1 are plotted in figure 22. We observe that both the power-law coefficient c_0 and the exponent c_1 decrease when gravity is introduced for $St \lesssim 1.5$ and increase when gravity is introduced for $St \gtrsim 1.5$, consistent with our explanations in § 4.2.1. The theoretical model for $g(r/\eta)$ from (4.15) (with the relative velocities and strain time scales specified from the DNS) is in good agreement with the DNS data, both with and without gravity. We also note that our DNS results for the exponent c_1 agree well with those of Rosa *et al.* (2013) and Bec *et al.* (2014) (not shown).

In Fouxon *et al.* (2015), the authors state that c_1 should be independent of St for large St and small Fr. This is generally consistent with our DNS results for $St \gtrsim 1$ in figure 22(*b*). They also argue that c_1 can be determined entirely from the fluid field as

$$c_1 = \frac{3\pi}{4} Fr \frac{\displaystyle\int_0^\infty \kappa E(\kappa)\, \mathrm{d}\kappa}{a_\eta}. \tag{4.21}$$

We include comparisons between our DNS results and the theoretical predictions of Fouxon *et al.* (2015) in figure 22(*b*). We see that (4.21) predicts c_1 to within about 50 % at high St. The model from (4.15), however, gives much more accurate quantitative predictions, but does require the second-order structure functions and the Lagrangian time scales for the inertial particles from the DNS.

To further investigate the two-parameter space of particle inertia and gravity, we consider the RDFs at $R_\lambda = 227$ for various St and Sv in figure 23. While the particle clustering behaviour here is generally complex and varies strongly with St and Sv,

https://doi.org/10.1017/jfm.2016.227 Published online by Cambridge University Press

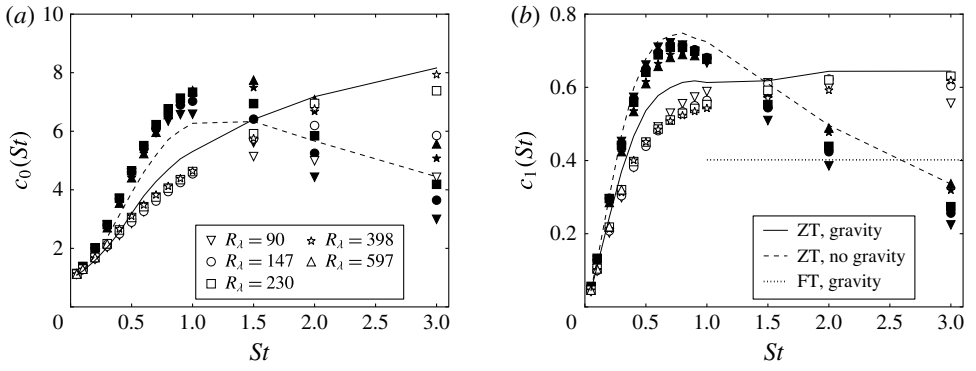

FIGURE 22. The (*a*) prefactor c_0 and the (*b*) exponent c_1 of the power-law fits of the RDFs using (4.20). Open symbols denote data with gravity ($Fr = 0.052$) and filled symbols denote data without gravity. The predictions from Zaichik & Alipchenkov (2009) for $R_\lambda = 398$ ('ZT', where DNS data are used to specify the relative velocities and the strain time scales here) are shown with solid lines (gravity) and dashed lines (no gravity). The theoretical high-St predictions from Fouxon *et al.* (2015) ('FT') for $R_\lambda = 398$ are also included in (*b*).

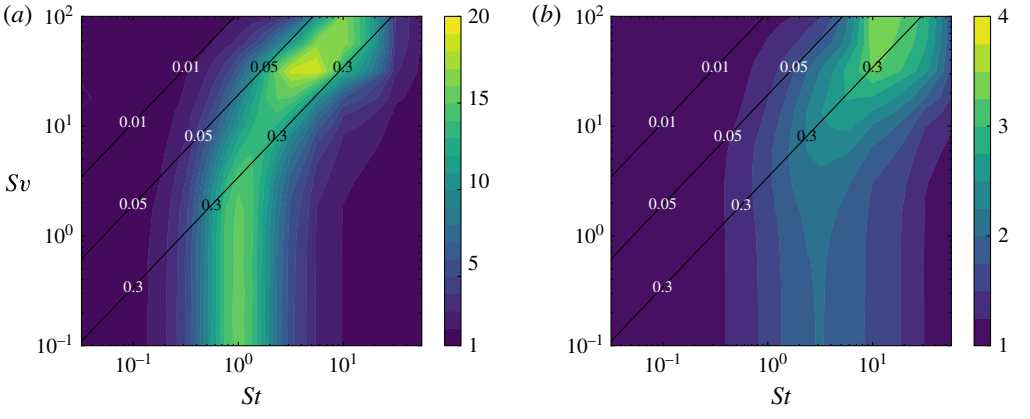

FIGURE 23. (Colour online) Filled contours of the RDF evaluated at $r/\eta = 0.25$ (*a*) and $r/\eta = 9.75$ (*b*) for different values of St and Sv, for $R_\lambda = 227$. The diagonal lines denote three different values of Fr, corresponding to conditions representative of stratiform clouds ($Fr = 0.01$), cumulus clouds ($Fr = 0.05$) and cumulonimbus clouds ($Fr = 0.3$).

we are able to provide physical explanations for several of the observed trends. For $St \gg 1$, the RDFs generally decrease with increasing St, since the particles become unresponsive to almost all of the underlying turbulence, as expected. Also, for $St \lesssim 1$, the RDFs tend to decrease with increasing Sv, since the preferential sampling and path-history mechanisms both act to increase clustering here, and they are both reduced by gravity. We also see that for $1 < St < 10$, the RDFs generally increase with increasing Sv, as expected, since gravity increases the ratio between the drift and the diffusion, as discussed in § 4.2.1.

https://doi.org/10.1017/jfm.2016.227 Published online by Cambridge University Press

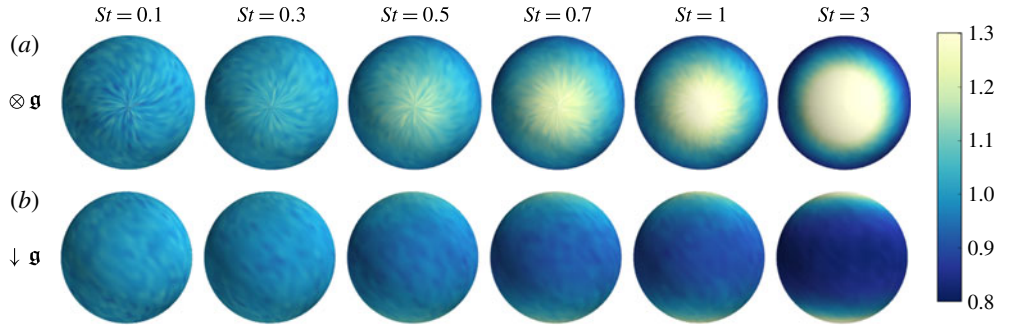

FIGURE 24. (Colour online) The ADF $g(\boldsymbol{r})$ (normalized by the RDF $g(r)$) shown on a unit sphere for $R_\lambda = 398$ and separations $r < \eta$ with gravity ($Fr = 0.052$). The different columns correspond to different values of St. (*a*) Shows the projection where gravity is directed into the page and (*b*) shows the projection where gravity is directed downward.

We now investigate the anisotropy of the particle field by introducing higher-order spherical harmonic functions,

$$\frac{g(\boldsymbol{r})}{g(r)} = \sum_{\ell=1}^{\infty} \frac{\mathscr{C}_{2\ell}^0(r)}{\mathscr{C}_0^0(r)} Y_{2\ell}^0(\theta), \tag{4.22}$$

in figure 24 for various values of St with gravity ($Fr = 0.052$) at $R_\lambda = 398$.

Consistent with the qualitative observations from figure 19, we see that particle clustering is strongest along the vertical direction, in agreement with earlier findings of Dejoan & Monchaux (2013), Bec *et al.* (2014) and Park & Lee (2014). At low St, the anisotropic clustering is caused by the fact that particles tend to preferentially sample downward-moving flow (see § 3.2). Bec *et al.* (2014) showed that this preferential sampling causes particles to form vertical clusters when St is small.

When St is large, the effects of preferential sampling vanish, and the anisotropy is related to the way gravity influences the path-history effect. Since the analysis presented in § 4.2.1 is restricted to spherically averaged clustering, the results cannot be used to predict the trends in anisotropy. However, we expect that the clustering anisotropy is linked to both the anisotropy in the relative velocities (see § 4.1.2) and the anisotropy in the strain and rotation time scales (see § 3.1). That is, directional variations in the relative velocities and the strain and rotation time scales will lead to directional variations in the ratio between drift and diffusion. This in turn will cause the particle clustering to be anisotropic. Indeed, the recent paper of Fouxon *et al.* (2015) argues that vertical clusters form at high St with gravity because the velocities of particle pairs have different correlation times in the horizontal and vertical directions. We hope that this and similar theories can be further developed and tested by using the anisotropic strain and rotation time scale results presented in § 3.1.

We also note that the anisotropy increases with increasing St. The physical explanation is that as St (and thus Sv) increases, gravitational forces become more significant, causing the particle motion to be more anisotropic. However, we expect that at some sufficiently large values of St and Sv, the particles are unaffected by the fluid turbulence, and thus clustering (and the associated anisotropy) will vanish.

We explore the degree of anisotropy as a function of the separation distance r and the Reynolds number by plotting the spherical harmonic coefficients $\mathscr{C}_2^0$ and $\mathscr{C}_4^0$ in

https://doi.org/10.1017/jfm.2016.227 Published online by Cambridge University Press

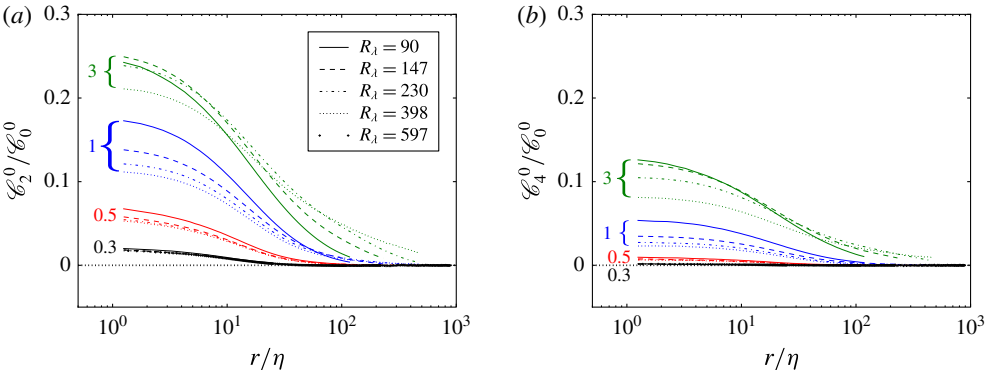

FIGURE 25. (Colour online) The second (a) and fourth (b) spherical harmonic coefficients of the angular distribution function normalized by the zeroth spherical harmonic coefficient, plotted as a function of r/η, for different St and R_λ with gravity ($Fr = 0.052$). The different values of St considered (0.3, 0.5, 1, 3) are shown in black, red, blue and green, respectively, and the Stokes numbers are indicated by the line labels.

figure 25 (coefficients above order four are too small to be statistically significant, and hence are not shown). In agreement with figure 19, we see that the anisotropy increases with increasing St. We also observe that as r/η increases, the anisotropy approaches zero, since both the clustering and the clustering anisotropy vanish in the limit $r/\eta \to \infty$.

The degree of anisotropy is also Reynolds-number dependent and decreases with increasing R_λ for larger values of St. Since the relative velocities of high-St particles generally also tend to become more isotropic as R_λ increases (see § 4.1.2), it is likely that the reduction in the anisotropy of the relative velocities will cause a similar reduction in the anisotropy of the clustering.

4.3. *Particle collision kernels*

The final two-particle statistic we consider is the kinematic collision kernel K for inertial particles. Sundaram & Collins (1997) and Wang, Wexler & Zhou (2000) showed that for an isotropic particle field, K is given by

$$K(d) = 4\pi d^2 g(d) S^p_{-\parallel}(d), \tag{4.23}$$

where d is the particle diameter. In appendix C, we show mathematically that (4.23) holds even for an anisotropic particle field. As in Part 1, we plot the non-dimensional collision kernel $\hat{K}(d) = K(d)/(d^2 u_\eta)$ in figure 26 (see also Voßkuhle *et al.* 2014). Note that while we simulate only point particles, we define d from St for this plot by prescribing the density ratio to be $\rho_p/\rho_f = 1000$. Since our statistics are generally not sufficient to compute the RDFs and relative velocities at separations of the order of the particle diameter, we fit both quantities using linear least-squares power-law regression and extrapolate the resulting power-law fits to $r = d$ (refer to Rosa *et al.* 2013).

Figure 26 shows the dimensionless collision kernel, with and without gravity, as a function of the Stokes number. Notice that the collision kernel is reduced by gravity. At low St, the RDF and the relative velocity both decrease with gravity, thereby decreasing the collision kernel. At higher St, the reduction in the relative velocity

https://doi.org/10.1017/jfm.2016.227 Published online by Cambridge University Press

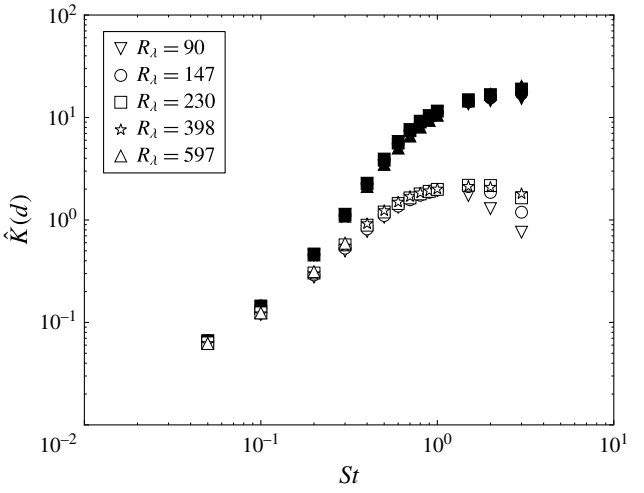

FIGURE 26. The non-dimensional collision kernel $\hat{K}(d)$ plotted as a function of St for $\rho_p/\rho_f = 1000$ and different values of R_λ. The open symbols denote data with gravity ($Fr = 0.052$), and the filled symbols denote data without gravity.

with gravity (see § 4.1.2) is sufficient to compensate for the slight increase in the RDF with gravity (see § 4.2.2), sustaining the net reduction in the collision kernel.

We next consider the dependence of the collision kernels on the Reynolds number. To make any dependencies more obvious, we divide the collision kernel at a given Reynolds number by the corresponding value at $R_\lambda = 90$ and plot the results in figure 27. At low St, we see almost no Reynolds-number dependence, since both the mean inward relative velocities (§ 4.1.2) and the RDFs (§ 4.2.2) are mostly independent of R_λ here. For $St > 1$, the collision rates increase with increasing R_λ, since both the relative velocity and RDF increase with increasing Reynolds number.

We found in Part 1 that $\hat{K}(d)$ without gravity is nearly independent of ρ_p/ρ_f for $St \gtrsim 1$, in agreement with Voßkuhle *et al.* (2014). The physical explanation is that $g(d)$ and $S^p_{-\parallel}(d)/u_\eta$ are either independent of d (for $St \geqslant 10$) or have inverse power-law scalings with d that precisely cancel (for $1 \lesssim St \leqslant 3$). In contrast, with gravity, path-history effects are suppressed, and these quantities have different scaling behaviours (see §§ 4.1.2 and 4.2.2). We therefore find that with gravity, $\hat{K}(d)$ decreases with increasing ρ_p/ρ_f at all values of St considered, as shown in figure 28.

Next, we expand our parameter space to consider the collision kernel for a wide range of St and Sv in figure 29. Here, we limit our analysis to cases where $\rho_p/\rho_f = 1000$. Once again, we caution that the statistics at the highest values of St and Sv may be affected by the periodic boundary conditions in the vertical direction (see appendix A), the use of a linear drag model (cf. § 2.2) and the extrapolations based on power-law fits that become questionable for $St > 3$. Nevertheless, the contour plot shown in figure 29 captures the qualitative trends of the collision kernel. In agreement with the discussion above, we see that the collision kernel generally increases with increasing St and decreases with increasing gravity. A practical implication is that at a given value of St, cumulonimbus clouds ($Fr \approx 0.3$) will have more frequent droplet collisions and growth than stratiform clouds ($Fr \approx 0.01$).

We now consider the anisotropic collision kernel, $K(r, \theta, \phi)$, defined as

$$K(d, \theta, \phi) \equiv 4\pi r^2 g(d, \theta, \phi) S^p_{-\parallel}(d, \theta, \phi). \tag{4.24}$$

https://doi.org/10.1017/jfm.2016.227 Published online by Cambridge University Press

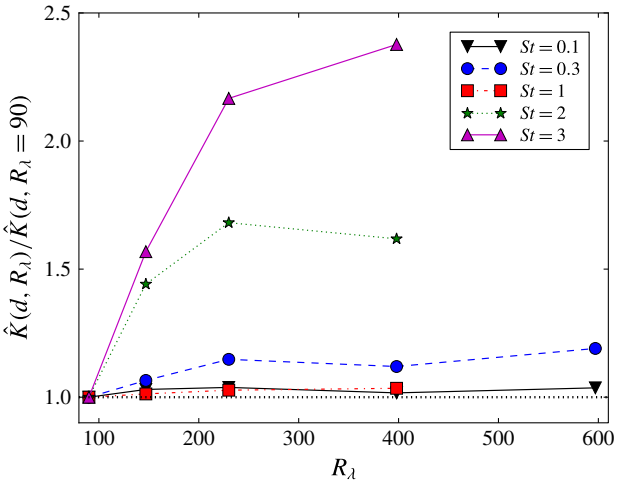

FIGURE 27. (Colour online) The ratio between $\hat{K}(d)$ at a given value of R_λ to that at $R_\lambda = 90$, to highlight the Reynolds-number dependence. All data are with gravity ($Fr = 0.052$) and for $\rho_p/\rho_f = 1000$.

$K(d, \theta, \phi)$ provides a measure of the rate at which particles with diameter d collide along an orientation defined by the radial angle θ and azimuthal angle ϕ. We plot the ratio between $K(d, \theta, \phi)$ and its spherical average in figure 30. (We are unable to show the anisotropic collision kernel at $r = d$ due to inadequate statistics at these small separations. We instead show data at $0 \leqslant r < \eta$, the smallest separation range over which adequate statistics are available.)

At low St, the collision kernel is approximately isotropic, since gravitational effects are weak. Interestingly, the collision kernel also tends toward isotropy at large St, due to the opposing trends in anisotropy of the relative velocities (see figure 17) and ADFs (see figure 24). For St between 0.1 and 1, particles are more likely to collide along the vertical direction, since both the ADFs and the relative velocities are strongest in the vertical direction for these values of St.

Before closing this section, we emphasize two practical implications of these collision results for the cloud physics community. The first is that since the DNS indicates that the collision rates of particles with low and moderate St are independent of R_λ, it is likely that the collision kernels computed here will be useful for predicting droplet collisions in high-Reynolds-number atmospheric clouds. The second is that gravity significantly reduces the collision kernels for $St \gtrsim 0.1$, which implies that simulations without gravity can significantly overpredict the collision rates of droplets in atmospheric clouds, and highlights the need to include gravity in the analysis of collisional droplet growth in turbulent clouds.

5. Conclusions

In this study, we explored the influence of gravity on inertial particle statistics in isotropic turbulence, with the goal of understanding the turbulence mechanisms contributing to droplet collisions. Our simulations were performed over the largest Reynolds-number range ($90 \leqslant R_\lambda \leqslant 597$), domain lengths ($\mathscr{L}/\ell \lesssim 40$) and range of particle classes ($0 \leqslant St \leqslant 56.2$, $0 \leqslant Sv \leqslant 100$) to date. We showed that such large

https://doi.org/10.1017/jfm.2016.227 Published online by Cambridge University Press

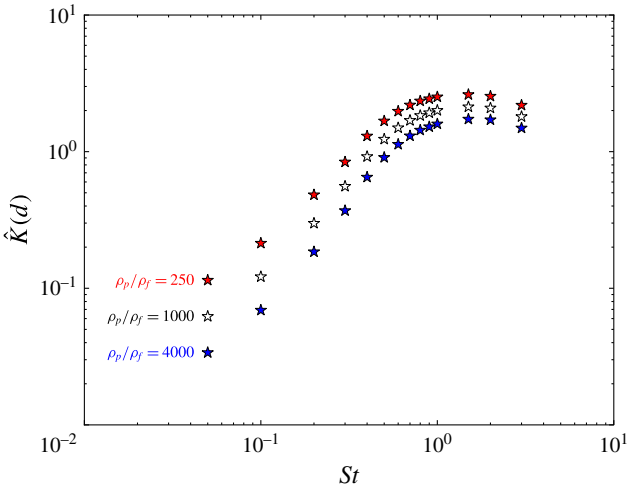

FIGURE 28. (Colour online) The non-dimensional collision kernel $\hat{K}(d)$ plotted as a function of St for different values of ρ_p/ρ_f and $R_\lambda = 398$. All data are with gravity. Filled red symbols indicate $\rho_p/\rho_f = 250$, open symbols indicate $\rho_p/\rho_f = 1000$ and filled blue symbols indicate $\rho_p/\rho_f = 4000$.

domain sizes are essential to obtain accurate statistics of settling inertial particles, suggesting that earlier published DNS studies may have errors due to the periodic boundary conditions in the vertical direction (see appendix A).

Our results indicate that preferential sampling affects the dynamics of particles with $St \ll 1$, both with and without gravity. Gravity decreases the degree of preferential sampling by reducing the time the particles have to interact with the underlying turbulent fields. In particular, gravity reduces the Lagrangian time scales for strain and rotation along particle trajectories. As gravitational forces increase, the particles fall more rapidly through the flow, leading to smaller velocities and larger accelerations than in the case without gravity. We developed models for the Lagrangian strain and rotation time scales along particle trajectories and the particle acceleration variances that are valid in the limit $Sv \gg u'/u_\eta$. The model predictions are in reasonable agreement with the DNS in this limit. We also find that the mean settling velocity is independent of R_λ at low St, in agreement with Bec *et al.* (2014).

We then applied this understanding of the gravity effect on single-particle statistics to two-particle statistics relevant for predicting the collision kernel. At high St, we observed that gravity reduces the particle relative velocities from their values without gravity by reducing the path-history effect. At low St, gravity acts primarily to reduce the degree of preferential sampling, causing the relative velocities at small separations to be closer to those of fluid particles.

Next, we relate the trends in the relative velocities to those in the particle clustering by considering the effect of gravity on a derivative model of the theoretical work of Zaichik & Alipchenkov (2009). With gravitational effects included, the model is able to predict the spherically averaged RDFs very accurately when DNS data is used to prescribe the relative velocities and the Lagrangian strain time scales. By analysing the model at low St, we see that the primary effect of gravity is to decrease the inward drift, leading to a decrease in the RDFs. At higher St, in contrast, gravity modulates both the inward drift and outward diffusion by diminishing the path-history effect in

https://doi.org/10.1017/jfm.2016.227 Published online by Cambridge University Press

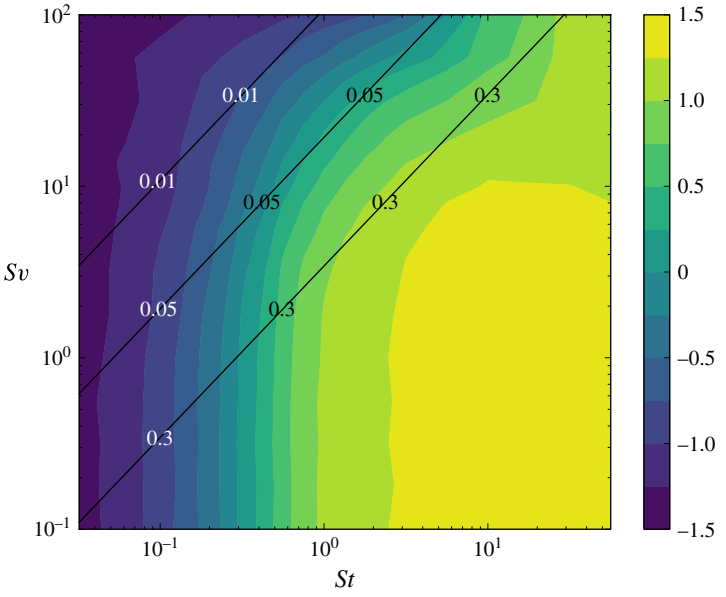

FIGURE 29. (Colour online) Filled contours of $\hat{K}(d)$ for different values of St and Sv at $R_\lambda = 227$ for $\rho_p/\rho_f = 1000$. The contours are logarithmically scaled, and the colour bar labels indicate the exponents of the decade. The diagonal lines denote three different values of Fr, corresponding to conditions representative of stratiform clouds ($Fr = 0.01$), cumulus clouds ($Fr = 0.05$) and cumulonimbus clouds ($Fr = 0.3$).

such a way as to increase the drift-to-diffusion ratio, causing an increase in clustering with gravity. We also find that the degree of clustering is only weakly dependent on R_λ at low St, but becomes increasingly sensitive to R_λ at higher St. The model captures both of these trends through its internal description of the path-history effects.

We also quantify the degree of anisotropy in these two-particle statistics using a spherical harmonic decomposition. Our results indicate that the particle angular distribution functions and radial relative velocities can have anisotropies of the order of 25 %, with the degree of anisotropy generally peaking at small r/η. At larger separations, the relative velocities induced by turbulence become comparatively larger, limiting the effect of gravity on particle dynamics.

We used these data for the RDFs and relative velocities to compute the particle collision kernel. As in Part 1, we find that the collision kernel is generally independent of R_λ at low St, while it increases with increasing R_λ at high St. We analyse the collision kernel using spherical harmonic decompositions, and find that the collision kernel is generally more isotropic than the ADFs and the mean inward relative velocities, since the anisotropies in the ADFs and the relative velocities have opposing trends at large St.

We conclude by highlighting some practical implications of this work for the cloud physics and turbulence communities and suggesting promising research directions. As in Part 1, the fact that the collision rates are generally independent of R_λ for droplet sizes representative of those in warm, cumulus clouds suggests that the collision rates predicted here (for $R_\lambda \lesssim 600$) may be representative of those found in atmospheric clouds ($R_\lambda \sim 10\,000$). Of course, more simulations at even higher Reynolds numbers would help to verify this conjecture, as would accurate experimental or atmospheric

https://doi.org/10.1017/jfm.2016.227 Published online by Cambridge University Press

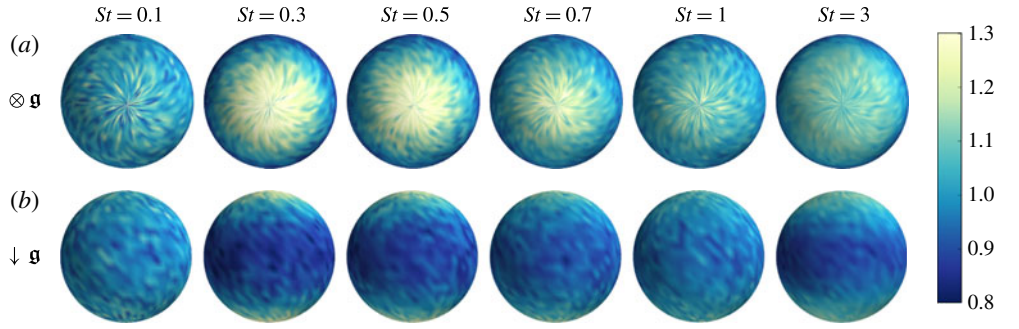

FIGURE 30. (Colour online) The anisotropic collision kernel $K(r, \theta, \phi)$ (normalized by the spherical average $K(r)$) shown on a unit sphere for $R_\lambda = 398$ and separations $r < \eta$ with gravity ($Fr = 0.052$). The different columns correspond to different values of St. (*a*) Shows the projection where gravity is directed into the page, and (*b*) shows the projection where gravity is directed downward.

measurements. Also, as noted in § 4.3, we observed that collision rates with gravity are considerably lower than without gravity, suggesting that earlier work that neglected gravity may have overpredicted the collision kernels.

While our study has focused on like-sized particles, our results suggest that gravity will have a significant effect on the collision kernels of unlike (different-sized) particles. For example, we observe that gravity tends to enhance the settling speeds of particles with low and intermediate values of St. The coupling between turbulence and gravity may thereby increase the relative velocities of unlike particles, leading to more frequent collisions. In addition, we find that gravity causes inertial particles in turbulence to experience large accelerations. Chun *et al.* (2005) found that large accelerations can contribute to higher relative velocities between unlike particles, leading to higher collision frequencies.

Finally, one especially promising finding of this study is that by extending the model of Zaichik & Alipchenkov (2009) and using DNS data to specify the Lagrangian strain time scales and relative velocities, we are able to accurately predict the RDFs both without gravity (as was also found in Bragg & Collins 2014*a*) and with gravity. As noted in Bragg & Collins (2014*b*), however, this model provides poor predictions of the relative velocities of particles with moderate-to-large inertia. Future work should therefore be directed at improving these relative velocity predictions, and at introducing nonlinear drag effects into both the theoretical models and future DNS simulations. In addition, while we developed a model for the strain and rotation time scales in the limit of large St with gravity, we generally require a model for all values of St. If accurate models can be developed for the relative velocities and the strain and rotation time scales over the entire range of St in atmospheric clouds, we would be able to use the theory of Zaichik & Alipchenkov (2009) to model the collision kernel accurately, both with and without gravity, without requiring any inputs from DNS.

Acknowledgements

The authors gratefully acknowledge G. Good, S. Pope and P. Sukheswalla for many helpful discussions. The work was supported by the National Science Foundation through CBET grants 0756510 and 0967349, and through a graduate

https://doi.org/10.1017/jfm.2016.227 Published online by Cambridge University Press

	I				II			III	
R_λ	88	90	90	90	140	145	147	226	230
N	128	256	512	1024	256	512	1024	512	1024
$\mathscr{L}$	2π	4π	8π	16π	2π	4π	8π	2π	4π
St_{crit}	1.06	2.06	4.26	8.55	1.39	2.69	5.55	1.78	3.39
ℓ	1.46	1.52	1.47	1.47	1.40	1.49	1.44	1.40	1.49
ℓ/η	55.8	57.7	55.7	55.6	106	111	107	202	213
u'	0.914	0.912	0.912	0.912	0.914	0.916	0.914	0.915	0.914
u'/u_η	4.77	4.81	4.82	4.82	6.01	6.12	6.15	7.60	7.70

TABLE 3. Simulation parameters for the periodicity study.

research fellowship to P.J.I. Additional funding was provided by Cornell University. Computational simulations were performed on Yellowstone (ark:/85065/d7wd3xhc) at the US National Center for Atmospheric Research (Computational and Information Systems Laboratory 2012) under grants ACOR0001 and P35091057, and on resources at the Max Planck Institute for Dynamics and Self-Organization. We are grateful to D. Flieger for assistance with the computational resources at the Max Planck Institute.

Appendix A. Periodicity effects

As noted in Woittiez *et al.* (2009), particle statistics in DNS may be artificially influenced by the periodicity of the domain when gravitational forces are strong. In particular, Woittiez *et al.* (2009) estimated that periodicity effects become significant when the time it takes a particle to fall through the domain ($\sim\mathscr{L}\tau_p^{-1}\mathfrak{g}^{-1}$) is less than the large eddy turnover time $T_L \equiv \ell/u'$, or equivalently, when

$$Sv = \frac{St}{Fr} \gtrsim \frac{\mathscr{L}}{\ell}\frac{u'}{u_\eta}. \tag{A 1}$$

In this case, a particle can artificially encounter the same large eddy multiple times due to the finite domain length. We define St_{crit} as the value of St at which $St/Fr = \mathscr{L}u'/(\ell u_\eta)$. This roughly corresponds to the largest Stokes number at which we can expect the results to be unaffected by periodicity.

To study the effects of periodicity, we systematically increased the domain size for the cases at the three lowest Reynolds numbers, while keeping the large scales, small scales and the forcing parameters the same. The simulation parameters are summarized in table 3. For convenience, we will hereafter refer to the simulations from groups I, II and III by their nominal Reynolds numbers of $R_\lambda \approx 90$, 147 and 230, respectively. In all cases, $0 \leqslant St \leqslant 3$ and $Fr = 0.052$.

The resulting energy spectra are shown in figure 31. In all cases, forcing is applied deterministically to wavenumbers with magnitude $\kappa = \sqrt{2}$, and thus the location of the peak in the spectra is approximately the same for all domain sizes. The spectra are nearly identical to the right of the peak, indicating that the inertial and dissipation range flow scales remain unchanged. We notice that as the domain size increases, larger-scale (i.e. lower-wavenumber) flow features become present. These features, however, account for very little of the overall energy, and thus they do not significantly affect the fluid statistics.

https://doi.org/10.1017/jfm.2016.227 Published online by Cambridge University Press

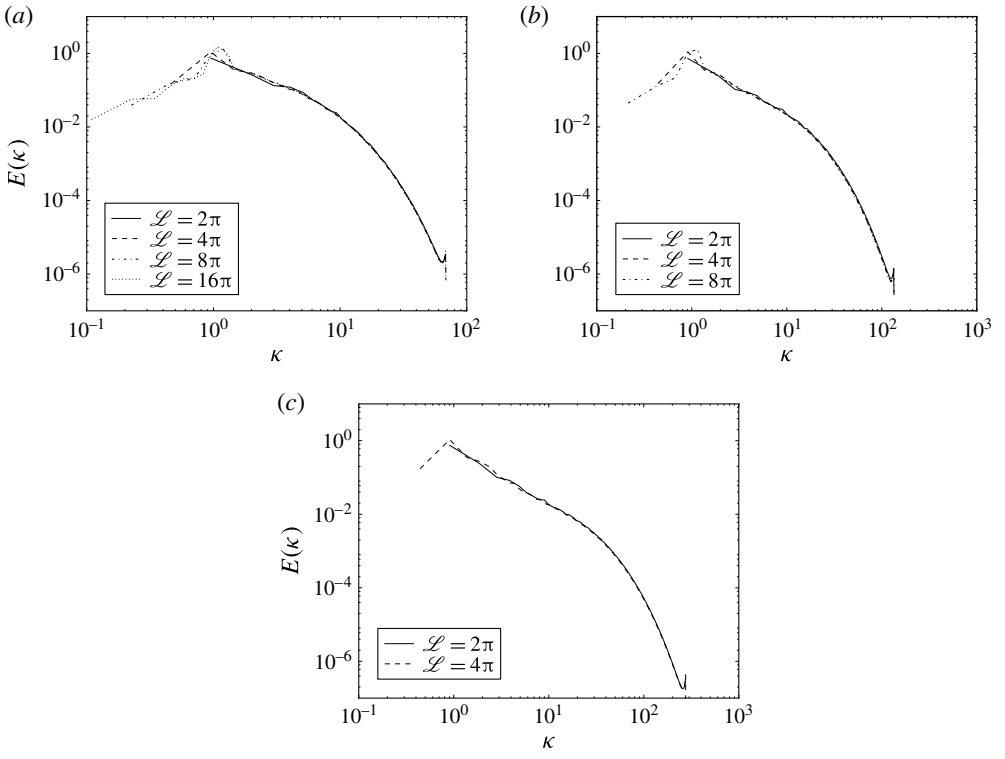

FIGURE 31. Energy spectra for different domain lengths $\mathscr{L}$ and nominal Reynolds numbers $R_\lambda = 90$ (*a*), $R_\lambda = 147$ (*b*) and $R_\lambda = 230$ (*c*). All values are in arbitrary units.

We first consider the effect of the domain size on the strain and rotation rates along particle trajectories. $\langle S^2\rangle^p$ and $\langle R^2\rangle^p$ (not shown) are generally invariant with changes in the domain size, since they are small-scale single-time quantities. The Lagrangian strain and rotation time scales in figure 32, however, appear to be overpredicted on the smaller domain sizes at large St. The explanation is that these time scales involve integrals of the autocorrelations of the strain and rotation components (see (3.1)), and artificially high correlations can result when a particle is wrapped around a domain boundary, increasing the time scales. At the highest values of St, our results suggest that the strain and rotation time scales have not yet converged to a grid-independent result, even though our scaling argument in (A 1) indicates that the Stokes numbers considered are generally well below St_{crit}. Since these time scales are very small ($\sim 0.1\tau_\eta$), their values can be significantly affected by very weak correlations induced by periodicity, and thus extremely large domain sizes may be necessary for these artificial correlations to vanish. We also see that our DNS time scales are considerably larger than the theoretical predictions from § B.1. While part of this discrepancy at large St is due to periodicity effects, it is also possible that the theory in § B.2 requires larger values of Sv than we are able to simulate here.

We next discuss the effect of periodicity on velocity and acceleration statistics. The turbulence-induced changes in the mean particle settling speeds (not shown) are generally independent of the domain size. This is presumably because the turbulence-induced settling speed modifications of large-St particles (which experience the strongest periodicity effects) are negligible, and thus the domain periodicity will

https://doi.org/10.1017/jfm.2016.227 Published online by Cambridge University Press

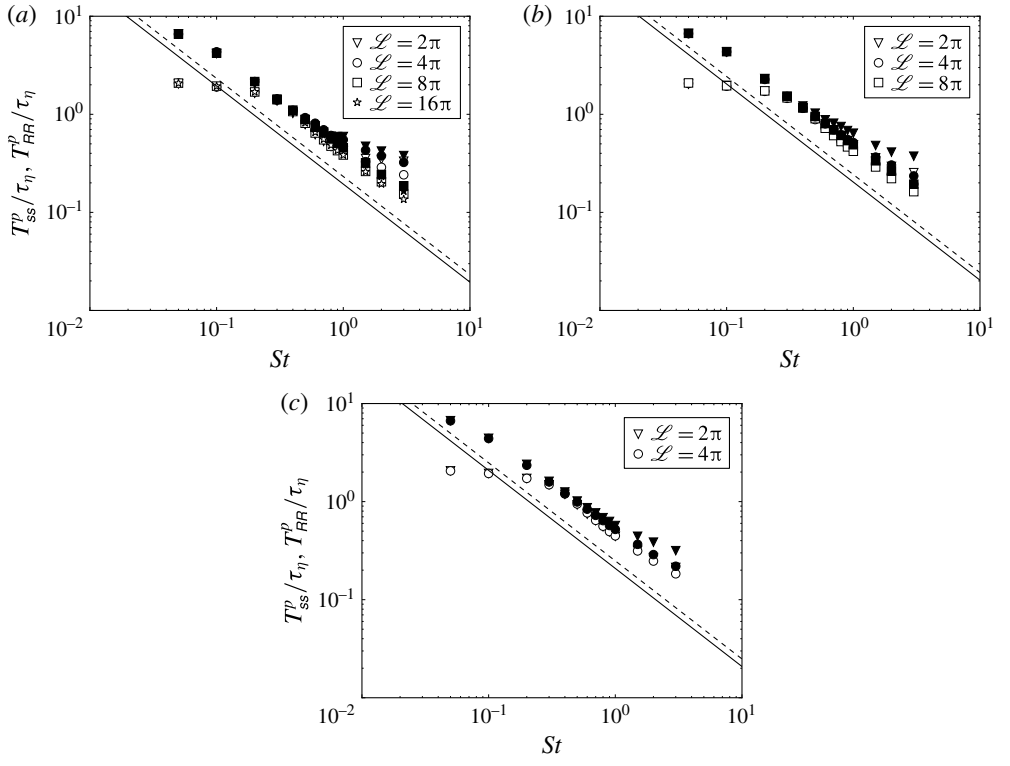

FIGURE 32. The Lagrangian strain (open symbols) and rotation (filled symbols) time scales for different domain lengths $\mathscr{L}$ and nominal Reynolds numbers $R_\lambda = 90$ (*a*), $R_\lambda = 147$ (*b*) and $R_\lambda = 230$ (*c*). The theoretical predictions for the strain and rotation time scales for $Sv \gg u'/u_\eta$ are shown with solid and dashed lines, respectively.

not lead to significant changes in this statistic. It is possible, however, that the settling speeds with a nonlinear drag model (which are reduced at large St, see Good *et al.* (2014)) will be affected by the domain size.

We show acceleration variance statistics in figure 33. The acceleration variances are underpredicted at the smallest domain sizes, and converge to the theoretical predictions at high St (see § B.2) as the domain size is increased. The vertical acceleration variances are more affected by the periodic boundary conditions than the horizontal acceleration variances, since the vertical velocities are correlated over longer length scales (as explained in § 3.3).

We conclude this section by examining the relative velocity statistics and the RDFs. Figures 34 and 35 show the mean inward relative velocities and relative velocity variances, respectively. These statistics are only weakly sensitive to the domain size for all St and converge to a grid-independent result. The relative velocity variances appear to be slightly more sensitive to the domain size than the mean inward relative velocities, presumably because the former are higher-order statistics and are thus sensitive to larger and more intermittent flow features.

Figure 36 indicates that the RDFs are almost entirely unaffected by the finite domain sizes at low St. At $St = 3$ (figure 37), however, the RDFs are evidently quite sensitive to the domain size, and do not converge to a grid-independent result. It is

https://doi.org/10.1017/jfm.2016.227 Published online by Cambridge University Press

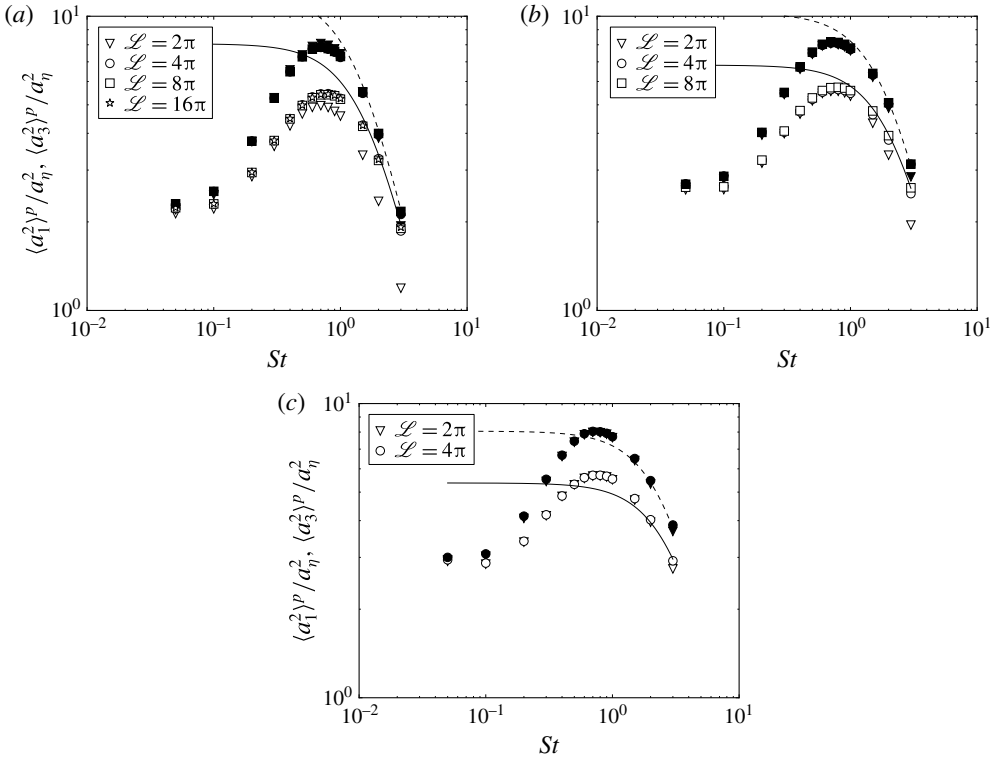

FIGURE 33. DNS data for $\langle a_1^2 \rangle^p / a_\eta^2$ (filled symbols) and $\langle a_3^2 \rangle^p / a_\eta^2$ (open symbols) for different domain lengths $\mathscr{L}$ and nominal Reynolds numbers $R_\lambda = 90$ (*a*), $R_\lambda = 147$ (*b*) and $R_\lambda = 230$ (*c*). The theoretical predictions for the horizontal (B 11) and vertical (B 12) acceleration variances for $Sv \gg u'/u_\eta$ are shown with dashed and solid lines, respectively.

possible that these RDFs are influenced by the small fraction of larger-scale features which appear as grid size is increased (see figure 31), or that the scaling argument in (A 1) is not sufficiently stringent for the RDF statistics. In any case, the results at large St should be interpreted with caution, since the linear drag model and the point-particle approximation are less accurate here (see § 2.2).

Appendix B. Theoretical models in the strong-gravity limit

In this section, we derive theoretical models that are expected to be valid in the limit of strong gravitational forces. We require two conditions for these models to hold. First, particles must fall so quickly that the spatial decorrelation of the turbulence along their trajectories occurs much faster than the Eulerian time scale of the flow. Second, a particle's displacement over a time s is to leading order equal to $\tau_p \mathfrak{g} s$.

The conditions can be shown to be satisfied when $Sv \gg u'/u_\eta$. It is important to note that $u'/u_\eta \sim R_\lambda^{1/2}$ in isotropic turbulence, which implies that our models will only hold for very large droplets (i.e. very large values of Sv) in high-Reynolds-number atmospheric clouds. In table 4, we provide an estimate of the droplet diameters d at which our model is expected to be valid for three different cloud types: stratiform clouds ($\epsilon \sim 10^{-3}$ m^2 s^{-3}), cumulus clouds ($\epsilon \sim 10^{-2}$ m^2 s^{-3}) and cumulonimbus clouds ($\epsilon \sim 10^{-1}$ m^2 s^{-3}).

https://doi.org/10.1017/jfm.2016.227 Published online by Cambridge University Press

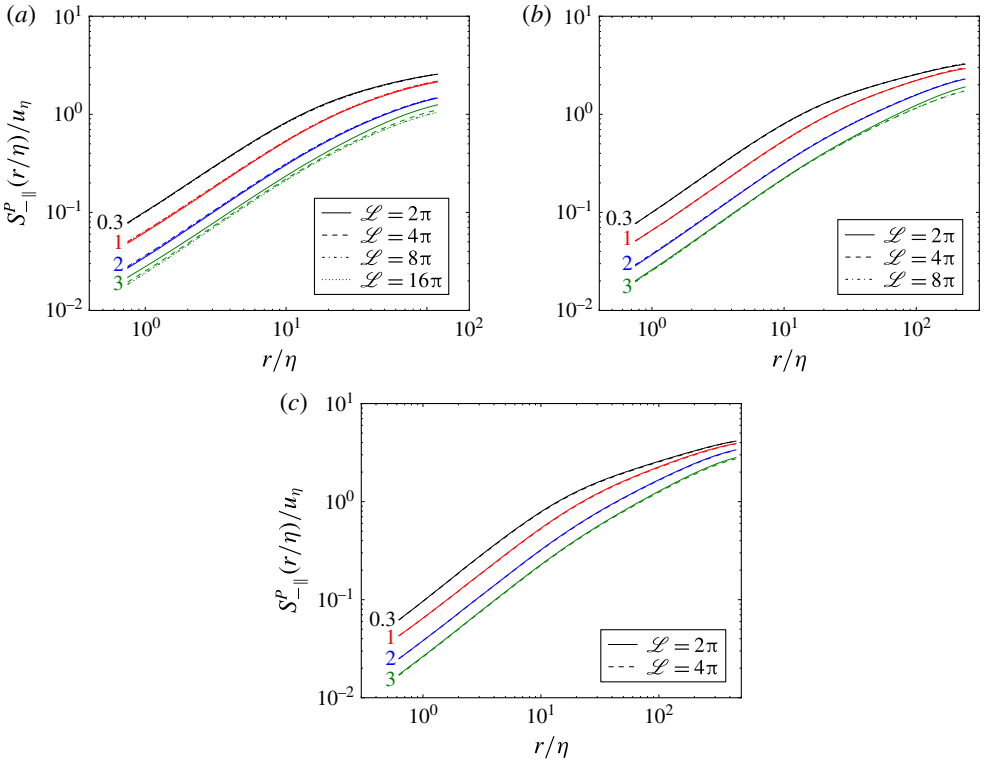

FIGURE 34. (Colour online) The mean inward relative velocities (normalized by u_η) for different domain lengths $\mathscr{L}$ for nominal Reynolds numbers $R_\lambda = 90$ (*a*), $R_\lambda = 147$ (*b*), and $R_\lambda = 230$ (*c*). The different Stokes numbers considered ($St = 0.3$, 1, 2, 3) are shown in black, red, blue and green, respectively, and the Stokes numbers are indicated by the line labels.

Cloud type	Stratiform	Cumulus	Cumulonimbus
ϵ (m^2 s^{-3})	10^{-3}	10^{-2}	10^{-1}
R_λ	10 800	15 900	23 300
u'/u_η	52.8	64.0	77.6
d (μm)	$\gg$127	$\gg$186	$\gg$273

TABLE 4. Estimated atmospheric cloud conditions at which our strong-gravity time scale model is expected to hold.

From table 4, we see that the droplet diameters at which these models are expected to be valid (of the order of hundreds to thousands of microns) are well above those of droplets in the 'size gap' in atmospheric clouds (between about 30 and 80 μm – see Part 1), where turbulence is expected to play a key role in droplet growth. However, while the models are not expected to yield accurate predictions of droplet dynamics in the size gap, they provide an important asymptotic limit in which to understand heavy-particle motion. Furthermore, since the Reynolds numbers in our simulations

https://doi.org/10.1017/jfm.2016.227 Published online by Cambridge University Press

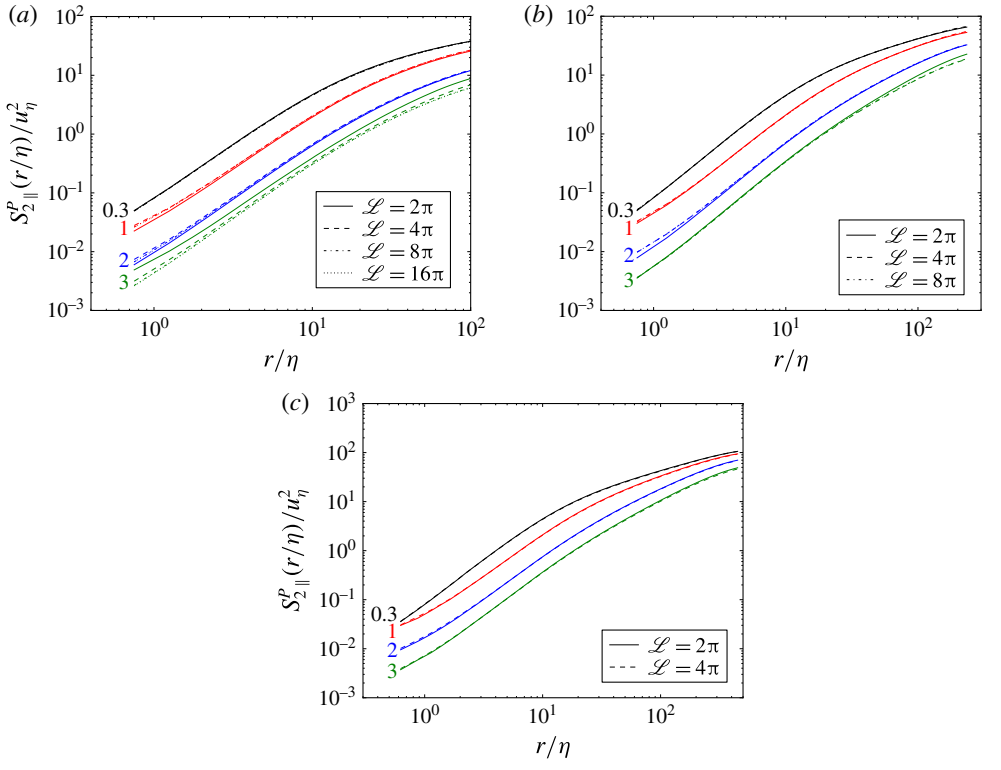

FIGURE 35. (Colour online) The parallel relative velocity variances (normalized by u_η^2) for different domain lengths $\mathscr{L}$ for nominal Reynolds numbers $R_\lambda = 90$ (*a*), $R_\lambda = 147$ (*b*) and $R_\lambda = 230$ (*c*). The different Stokes numbers considered ($St = 0.3$, 1, 2, 3) are shown in black, red, blue and green, respectively, and the Stokes numbers are indicated by the line labels.

are well below those in atmospheric clouds, we expect the models to agree well with our simulation data at the largest values of Sv.

In § B.1, we develop a model for the Lagrangian strain and rotation time scales of the flow seen by inertial particles and in § B.2, we model the particle accelerations.

B.1. *Lagrangian strain and rotation time scales along particle trajectories*

In the limit $Sv \gg u'/u_\eta$, we can model the Lagrangian strain time scale $T^p_{\mathsf{S}_{ij}\mathsf{S}_{km}}$ as

$$T^p_{\mathsf{S}_{ij}\mathsf{S}_{km}} = \frac{1}{\langle \mathsf{S}_{ij}(\mathbf{0},0)\mathsf{S}_{km}(\mathbf{0},0)\rangle}\int_0^\infty \int_{\boldsymbol{X}} \langle \mathsf{S}_{ij}(\boldsymbol{X},s)\mathsf{S}_{km}(\mathbf{0},0)\rangle \varrho(\boldsymbol{X},s)\,\mathrm{d}\boldsymbol{X}\,\mathrm{d}s, \tag{B 1}$$

where $\varrho(\boldsymbol{X},s) \equiv \delta(\boldsymbol{X} - \tau_p \mathbf{g} s)$. Here and through the rest of this section, no summation is implied by repeated indices in the time scale expressions.

Note that (B 1) is constructed by assuming that the turbulence evaluated along the particle trajectories is uncorrelated with the trajectory itself (i.e. 'Corrsin's hypothesis', see Corrsin 1963). In the limit $Sv \gg u'/u_\eta$, Corrsin's hypothesis is expected to become exact, since the particle motions are almost independent of the underlying flow field here.

https://doi.org/10.1017/jfm.2016.227 Published online by Cambridge University Press

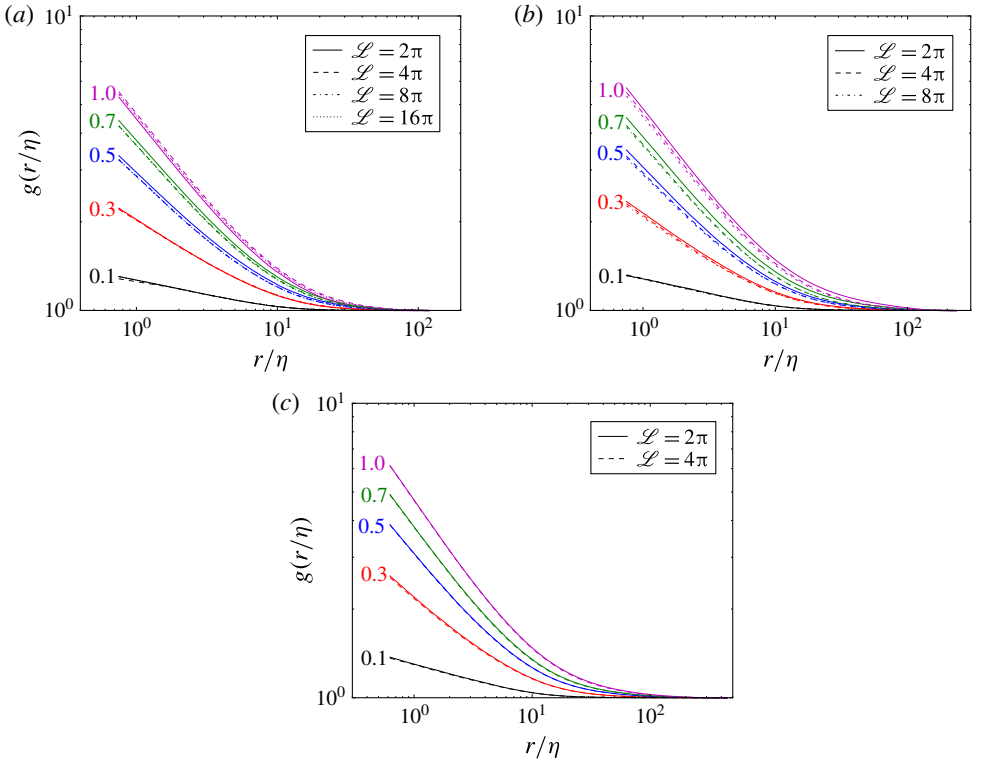

FIGURE 36. (Colour online) RDFs for different domain lengths $\mathscr{L}$ for nominal Reynolds numbers $R_\lambda = 90$ (*a*), $R_\lambda = 147$ (*b*) and $R_\lambda = 230$ (*c*). Data are shown for $St \leqslant 1$, with the Stokes numbers indicated by the line labels. The different Stokes numbers considered ($St = 0.1, 0.3, 0.5, 0.7, 1$) are shown in black, red, blue, green and magenta, respectively, and the Stokes numbers are indicated by the line labels.

Taking the integral of (B 1), we obtain

$$T^p_{S_{ij}S_{km}} = \frac{1}{\langle S_{ij}(\mathbf{0},0)S_{km}(\mathbf{0},0)\rangle}\int_0^\infty \langle S_{ij}(\tau_p \mathbf{g}s,0)S_{km}(\mathbf{0},0)\rangle \,\mathrm{d}s. \tag{B 2}$$

To derive an analytical expression for the time scales, we assume that $\langle S_{ij}(\tau_p \mathbf{g}s,0)S_{km}(\mathbf{0},0)\rangle$ decorrelates exponentially, which gives us

$$T^p_{S_{ij}S_{km}} = \ell_{S_{ij}S_{km},3}/(\tau_p g). \tag{B 3}$$

Here, $\ell_{S_{ij}S_{km},3}$ is the integral length scale of $S_{ij}S_{km}$ evaluated along the x_3-direction. We express (B 3) in non-dimensional form,

$$\hat{T}^p_{S_{ij}S_{km}} = \frac{\hat{\ell}_{S_{ij}S_{km},3}}{Sv}, \tag{B 4}$$

where we have used the top-hat symbol to denote a variable normalized by Kolmogorov scales. The rotation time scales $T^p_{R_{ij}R_{km}}$ are defined analogously,

$$\hat{T}^p_{R_{ij}R_{km}} = \frac{\hat{\ell}_{R_{ij}R_{km},3}}{Sv}. \tag{B 5}$$

https://doi.org/10.1017/jfm.2016.227 Published online by Cambridge University Press

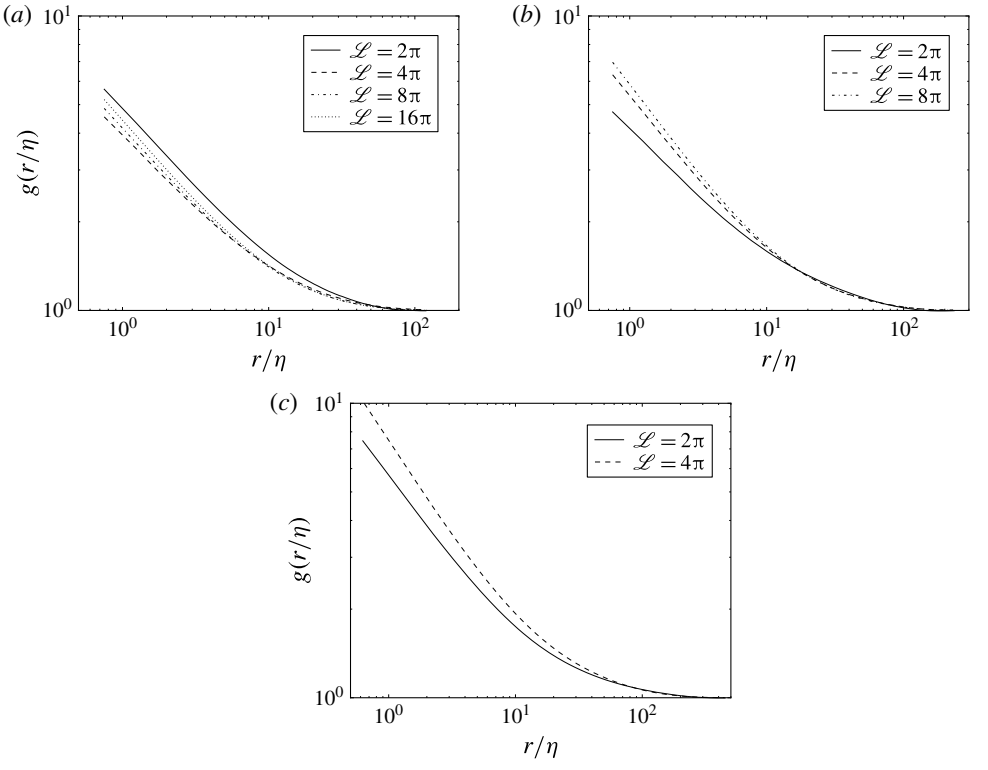

FIGURE 37. RDFs for different domain lengths $\mathscr{L}$ for nominal Reynolds numbers $R_\lambda = 90$ (*a*), $R_\lambda = 147$ (*b*) and $R_\lambda = 230$ (*c*). Data are shown for $St = 3$.

B.2. *Inertial particle acceleration variances*

We now develop a model for the particle acceleration variances in the limit $Sv \gg u'/u_\eta$. Following Bec *et al.* (2006), we write the formal solution for the particle acceleration as

$$\boldsymbol{a}^p(t) = \frac{1}{\tau_p^2}\int_{-\infty}^{t} \exp\left[\frac{s-t}{\tau_p}\right]\left[\boldsymbol{u}(\boldsymbol{x}^p(t), t) - \boldsymbol{u}(\boldsymbol{x}^p(s), s)\right] \mathrm{d}s. \tag{B 6}$$

Without loss of generality, we take $t = 0$ and write the particle acceleration covariance tensor $\langle \boldsymbol{a}^p(0)\boldsymbol{a}^p(0)\rangle$ as

$$\begin{aligned}\langle \boldsymbol{a}^p(0)\boldsymbol{a}^p(0)\rangle \;=\; & \frac{1}{\tau_p^4}\left\langle \boldsymbol{u}(\boldsymbol{x}^p(0), 0)\boldsymbol{u}(\boldsymbol{x}^p(0), 0)\int_{-\infty}^{0}\int_{-\infty}^{0} \exp\left[\frac{s}{\tau_p}\right]\exp\left[\frac{S}{\tau_p}\right] \mathrm{d}s\,\mathrm{d}S\right\rangle \\ & - \frac{2}{\tau_p^4}\left\langle \boldsymbol{u}(\boldsymbol{x}^p(0), 0)\int_{-\infty}^{0}\int_{-\infty}^{0} \exp\left[\frac{s}{\tau_p}\right]\exp\left[\frac{S}{\tau_p}\right]\boldsymbol{u}(\boldsymbol{x}^p(s), s)\,\mathrm{d}s\,\mathrm{d}S\right\rangle \\ & + \frac{1}{\tau_p^4}\left\langle \int_{-\infty}^{0}\int_{-\infty}^{0} \exp\left[\frac{s}{\tau_p}\right]\exp\left[\frac{S}{\tau_p}\right]\boldsymbol{u}(\boldsymbol{x}^p(s), s)\boldsymbol{u}(\boldsymbol{x}^p(S), S)\,\mathrm{d}s\,\mathrm{d}S\right\rangle. \end{aligned} \tag{B 7}$$

https://doi.org/10.1017/jfm.2016.227 Published online by Cambridge University Press

By assuming that preferential concentration effects are weak, we can approximate the first term on the right-hand side of (B 7) as

$$\tau_p^{-2}\langle \boldsymbol{u}(\boldsymbol{x}^p(0),0)\boldsymbol{u}(\boldsymbol{x}^p(0),0)\rangle \approx \frac{u'^2}{\tau_p^2}\boldsymbol{I}. \tag{B 8}$$

Based on PDF theory (Reeks 1993), the second term on the right-hand side of (B 7) is equivalent to the particle velocity covariance multiplied by $-2\tau_p^{-2}$, while the third term equivalent to the particle velocity covariance multiplied by τ_p^{-2}.

For $Sv \gg u'/u_\eta$, we can simplify the relations for the velocity covariances presented in Wang & Stock (1993) to obtain

$$\frac{\langle v_1^p(t)v_1^p(t)\rangle}{u'^2} = \frac{2+StSv(\eta/\ell)}{2[1+StSv(\eta/\ell)]^2}, \tag{B 9}$$

and

$$\frac{\langle v_3^p(t)v_3^p(t)\rangle}{u'^2} = \frac{1}{1+StSv(\eta/\ell)}. \tag{B 10}$$

From these relations, we write the horizontal and vertical particle acceleration variances as

$$\frac{\langle a_1^2\rangle^p}{a_\eta^2} = \left[\frac{u'}{u_\eta}\right]^2\left[\frac{Sv}{St}\right]\left[\frac{2StSv+3\left(\dfrac{\ell}{\eta}\right)}{2\left(StSv+\dfrac{\ell}{\eta}\right)^2}\right], \tag{B 11}$$

and

$$\frac{\langle a_3^2\rangle^p}{a_\eta^2} = \left[\frac{u'}{u_\eta}\right]^2\left[\frac{Sv}{St}\right]\left[\frac{1}{StSv+\dfrac{\ell}{\eta}}\right], \tag{B 12}$$

respectively.

Appendix C. Kinematic collision kernel for an anisotropic particle phase

In this section, we extend the derivation of Sundaram & Collins (1997) to determine the kinematic collision kernel formulation for an anisotropic particle phase. From Sundaram & Collins (1997), we write the average number of collisions per unit volume over a time period τ as

$$Z_c(\tau) = \frac{n^2}{2}\int_{\boldsymbol{w}}\int_{\boldsymbol{r}} \boldsymbol{\Phi}(\boldsymbol{r},\boldsymbol{w},\tau)p(\boldsymbol{r},\boldsymbol{w})\,\mathrm{d}\boldsymbol{r}\,\mathrm{d}\boldsymbol{w}, \tag{C 1}$$

where n is the particle number density, $\boldsymbol{\Phi}(\boldsymbol{r},\boldsymbol{w},\tau)$ is the collision operator and $p(\boldsymbol{r},\boldsymbol{w})$ is the joint PDF of the particle-pair separation and relative velocity. At this stage, it is simpler to leave the PDF as is rather than split it into a conditional average and the RDF as was done in Sundaram & Collins (1997). The collision kernel is given as

$$K(d) = \frac{2}{n^2}\lim_{\tau\to 0}\frac{Z_c(\tau)}{\tau} = \frac{2}{n^2}\frac{\mathrm{d}}{\mathrm{d}\tau}Z_c(0), \tag{C 2}$$

https://doi.org/10.1017/jfm.2016.227 Published online by Cambridge University Press

or equivalently,

$$\begin{aligned} K(d) &= \int_{\boldsymbol{w}}\int_{\boldsymbol{r}} -\frac{\boldsymbol{r}\cdot\boldsymbol{w}}{r(0)} H(t^*)\delta[d-r(0)]p(\boldsymbol{r},\boldsymbol{w})\,\mathrm{d}\boldsymbol{r}\,\mathrm{d}\boldsymbol{w} \\ &= \int_{\boldsymbol{r}} -H(t^*)\delta[d-r(0)]\frac{\boldsymbol{r}}{r(0)}\cdot\int_{\boldsymbol{w}}\boldsymbol{w}p(\boldsymbol{r},\boldsymbol{w})\,\mathrm{d}\boldsymbol{w}\,\mathrm{d}\boldsymbol{r} \\ &= \int_{\boldsymbol{r}} -H(t^*)\delta[d-r(0)]\frac{\boldsymbol{r}}{r(0)}\cdot\varrho\langle\boldsymbol{w}^p(t)\rangle_{\boldsymbol{r}}\,\mathrm{d}\boldsymbol{r}. \end{aligned} \tag{C 3}$$

In the above equations, t^* denotes the time required to reach the minimum particle separation, H is the Heaviside function, δ is the Dirac delta function and ϱ is the particle-pair PDF.

From the definition of t^* in Sundaram & Collins (1997), we require $\boldsymbol{r}\cdot\boldsymbol{w}\leqslant 0$ for $H(t^*)\geqslant 0$. Since

$$\boldsymbol{r}\cdot\langle\boldsymbol{w}^p(t)\rangle_{\boldsymbol{r}} \equiv \langle\boldsymbol{r}^p(t)\cdot\boldsymbol{w}^p(t)\rangle_{\boldsymbol{r}}, \tag{C 4}$$

then in order to satisfy $H(t^*)\geqslant 0$, we replace

$$\frac{\boldsymbol{r}}{r(0)}\cdot\varrho\langle\boldsymbol{w}^p(t)\rangle_{\boldsymbol{r}}, \tag{C 5}$$

with

$$-\frac{\boldsymbol{r}}{r(0)}\cdot\varrho\langle\boldsymbol{w}^{p-}(t)\rangle_{\boldsymbol{r}}, \tag{C 6}$$

where

$$\varrho\langle\boldsymbol{w}^{p-}(t)\rangle_{\boldsymbol{r}} \equiv -\int_{-\infty}^{\boldsymbol{0}}\boldsymbol{w}p(\boldsymbol{r},\boldsymbol{w})\,\mathrm{d}\boldsymbol{w}. \tag{C 7}$$

Furthermore, since

$$\frac{\boldsymbol{r}}{r(0)}\cdot\varrho\langle\boldsymbol{w}^{p-}(t)\rangle_{\boldsymbol{r}} = \frac{1}{r(0)}\varrho\langle\boldsymbol{r}^p(t)\cdot\boldsymbol{w}^{p-}(t)\rangle_{\boldsymbol{r}} = \frac{r}{r(0)}\varrho S^p_{-\parallel}(\boldsymbol{r}), \tag{C 8}$$

and we are considering the limit $\tau\to 0$ (in which $r(0)\to r$), we have

$$K(d) = \int_{\boldsymbol{r}}\delta[d-r]\varrho S^p_{-\parallel}(\boldsymbol{r})\,\mathrm{d}\boldsymbol{r}. \tag{C 9}$$

Since we are interested in collisions on a sphere, we write (C 9) in spherical coordinates by replacing $\boldsymbol{r}$ with (r,θ,ϕ) and $d\boldsymbol{r}$ with $r^2\sin\theta\,\mathrm{d}r\,\mathrm{d}\theta\,\mathrm{d}\phi$. This gives us

$$\begin{aligned} K(d) &= \int_r\int_0^{2\pi}\int_0^{\pi}\delta[d-r]\varrho S^p_{-\parallel}(r,\theta,\phi)r^2\sin\theta\,\mathrm{d}\theta\,\mathrm{d}\phi \\ &= d^2\int_0^{2\pi}\int_0^{\pi} g(d,\theta,\phi)S^p_{-\parallel}(d,\theta,\phi)\sin\theta\,\mathrm{d}\theta\,\mathrm{d}\phi. \end{aligned} \tag{C 10}$$

For an isotropic particle phase, we recover the expected result,

$$K(d) = 4\pi d^2 g(d) S^p_{-\parallel}(d), \tag{C 11}$$

where

$$g(d) = \frac{1}{4\pi}\int_0^{2\pi}\int_0^{\pi} g(d,\theta,\phi)\sin\theta\,\mathrm{d}\theta\,\mathrm{d}\phi, \tag{C 12}$$

https://doi.org/10.1017/jfm.2016.227 Published online by Cambridge University Press

and

$$S^p_{-\parallel}(d) = \frac{1}{4\pi}\int_0^{2\pi}\int_0^{\pi} S^p_{-\parallel}(d,\theta,\phi)\sin\theta\,\mathrm{d}\theta\,\mathrm{d}\phi. \tag{C 13}$$

For an anisotropic particle phase, however, (C 13) no longer holds. Note that $S^p_{-\parallel}(d)$ is an average over particle pairs on the entire surface of the sphere, while $S^p_{-\parallel}(d,\theta,\phi)$ is an average over particle pairs on a differential element of the sphere. When the particle phase is anisotropic, we must compute $S^p_{-\parallel}(d)$ by weighting each of the averages on the differential elements $S^p_{-\parallel}(d,\theta,\phi)$ by the number of particle pairs contributing to that average. In this case, we have

$$S^p_{-\parallel}(d) = \frac{1}{4\pi}\int_0^{2\pi}\int_0^{\pi} S^p_{-\parallel}(d,\theta,\phi)\frac{g(d,\theta,\phi)}{g(d)}\sin\theta\,\mathrm{d}\theta\,\mathrm{d}\phi, \tag{C 14}$$

which reduces to (C 13) for an isotropic particle phase. From (C 14), we can therefore show that

$$4\pi d^2 g(d) S^p_{-\parallel}(d) = d^2\int_0^{2\pi}\int_0^{\pi} g(d,\theta,\phi)S^p_{-\parallel}(d,\theta,\phi)\sin\theta\,\mathrm{d}\theta\,\mathrm{d}\phi, \tag{C 15}$$

which is precisely the result we derived in (C 10) for the anisotropic collision kernel. We have therefore demonstrated mathematically that (C 11) holds for both isotropic and anisotropic particle phases. This explains the empirical observations in Ayala *et al.* (2008), from which the authors argue that (C 11) holds even when the particle distribution is anisotropic.

REFERENCES

Abrahamson, J. 1975 Collision rates of small particles in a vigorously turbulent fluid. *Chem. Engng Sci.* **30**, 1371–1379.

Alipchenkov, V. M. & Beketov, A. I. 2013 On clustering of aerosol particles in homogeneous turbulent shear flows. *J. Turbul.* **14** (5), 1–9.

Aliseda, A., Cartellier, A., Hainaux, F. & Lasheras, J. C. 2002 Effect of preferential concentration on the settling velocity of heavy particles in homogeneous isotropic turbulence. *J. Fluid Mech.* **468**, 77–105.

Ayala, O., Rosa, B., Wang, L.-P. & Grabowski, W. W. 2008 Effects of turbulence on the geometric collision rate of sedimenting droplets. Part 1: results from direct numerical simulation. *New J. Phys.* **10**, 075015.

Ayyalasomayajula, S., Gylfason, A., Collins, L. R., Bodenschatz, E. & Warhaft, Z. 2006 Lagrangian measurements of inertial particle accelerations in grid generated wind tunnel turbulence. *Phys. Rev. Lett.* **97**, 144507.

Bec, J., Biferale, L., Boffetta, G., Celani, A., Cencini, M., Lanotte, A. S., Musacchio, S. & Toschi, F. 2006 Acceleration statistics of heavy particles in turbulence. *J. Fluid Mech.* **550**, 349–358.

Bec, J., Homann, H. & Ray, S. S. 2014 Gravity-driven enhancement of heavy particle clustering in turbulent flow. *Phys. Rev. Lett.* **112**, 184501.

Bragg, A. D. & Collins, L. R. 2014*a* New insights from comparing statistical theories for inertial particles in turbulence: I. Spatial distribution of particles. *New J. Phys.* **16**, 055013.

Bragg, A. D. & Collins, L. R. 2014*b* New insights from comparing statistical theories for inertial particles in turbulence: II: relative velocities. *New J. Phys.* **16**, 055014.

Bragg, A. D., Ireland, P. J. & Collins, L. R. 2015*a* Mechanisms for the clustering of inertial particles in the inertial range of isotropic turbulence. *Phys. Rev.* E **92**, 023029.

https://doi.org/10.1017/jfm.2016.227 Published online by Cambridge University Press

BRAGG, A. D., IRELAND, P. J. & COLLINS, L. R. 2015*b* On the relationship between the non-local clustering mechanism and preferential concentration. *J. Fluid Mech.* **780**, 327–343.

CHUN, J., KOCH, D. L., RANI, S., AHLUWALIA, A. & COLLINS, L. R. 2005 Clustering of aerosol particles in isotropic turbulence. *J. Fluid Mech.* **536**, 219–251.

CLIFT, R., GRACE, J. R. & WEBER, M. E. 1978 *Bubbles, Drops, and Particles*. Academic.

Computational and Information Systems Laboratory 2012 Yellowstone: IBM iDataPlex System (University Community Computing) http://n2t.net/ark:/85065/d7wd3xhc.

CORRSIN, S. 1963 Estimates of the relations between Eulerian and Lagrangian scales in large Reynolds number turbulence. *J. Atmos. Sci.* **20**, 115–119.

CSANADY, G. T. 1963 Turbulent diffusion of heavy particles in the atmosphere. *J. Atmos. Sci.* **20**, 201–208.

DÁVILA, J. & HUNT, J. C. R. 2001 Settling of small particles near vortices and in turbulence. *J. Fluid Mech.* **440**, 117–145.

DEJOAN, A. & MONCHAUX, R. 2013 Preferential concentration and settling of heavy particles in homogeneous turbulence. *Phys. Fluids* **25**, 013301.

DEVENISH, B. J., BARTELLO, P., BRENGUIER, J.-L., COLLINS, L. R., GRABOWSKI, W. W., IJZERMANS, R. H. A., MALINOWSKI, S. P., REEKS, M. W., VASSILICOS, J. C., WANG, L.-P. *et al.* 2012 Droplet growth in warm turbulent clouds. *Q. J. R. Meteorol. Soc.* **138**, 1401–1429.

EATON, J. K. & FESSLER, J. R. 1994 Preferential concentration of particles by turbulence. *Intl J. Multiphase Flow* **20**, 169–209.

ELGHOBASHI, S. E. & TRUESDELL, G. C. 1992 Direct simulation of particle dispersion in a decaying isotropic turbulence. *J. Fluid Mech.* **242**, 655–700.

ELGHOBASHI, S. E. & TRUESDELL, G. C. 1993 On the two-way interaction between homogeneous turbulence and dispersed particles. I: turbulence modification. *Phys. Fluids* A **5**, 1790–1801.

FOUXON, I., PARK, Y., HARDUF, R. & LEE, C. 2015 Inhomogeneous distribution of water droplets in cloud turbulence. *Phys. Rev.* E **92**, 033001.

FRANKLIN, C. N., VAILLANCOURT, P. A. & YAU, M. K. 2007 Statistics and parameterizations of the effect of turbulence on the geometric collision kernel of cloud droplets. *J. Atmos. Sci.* **64**, 938–954.

GERASHCHENKO, S., SHARP, N. S., NEUSCAMMAN, S. & WARHAFT, Z. 2008 Lagrangian measurements of inertial particle accelerations in a turbulent boundary layer. *J. Fluid Mech.* **617**, 255–281.

GHOSH, S., DÁVILA, J., HUNT, J. C. R., SRDIC, A., FERNANDO, H. H. S. & JONAS, P. R. 2005 How turbulence enhances coalescence of settling particles with applications to rain in clouds. *Proc. R. Soc. Lond.* A **461**, 3059–3088.

GOOD, G. H., IRELAND, P. J., BEWLEY, G. P., BODENSCHATZ, E., COLLINS, L. R. & WARHAFT, Z. 2014 Settling regimes of inertial particles in isotropic turbulence. *J. Fluid Mech.* **759**, R3.

GRABOWSKI, W. W. & WANG, L.-P. 2013 Growth of cloud droplets in a turbulent environment. *Annu. Rev. Fluid Mech.* **45**, 293–324.

GUALTIERI, P., PICANO, F. & CASCIOLA, C. M. 2009 Anisotropic clustering of inertial particles in homogeneous shear flow. *J. Fluid Mech.* **629**, 25–39.

GUSTAVSSON, K., VAJEDI, S. & MEHLIG, B. 2014 Clustering of particles falling in a turbulent flow. *Phys. Rev. Lett.* **112**, 214501.

VAN HINSBERG, M. A. T., THIJE BOONKKAMP, J. H. M., TOSCHI, F. & CLERCX, H. J. H. 2012 On the efficiency and accuracy of interpolation methods for spectral codes. *SIAM J. Sci. Comput.* **34** (4), B479–B498.

IRELAND, P. J., BRAGG, A. D. & COLLINS, L. R. 2016 The effect of Reynolds number on inertial particle dynamics in isotropic turbulence. Part 1. Simulations without gravitational effects. *J. Fluid Mech.* **796**, 617–658.

IRELAND, P. J. & COLLINS, L. R. 2012 Direct numerical simulation of inertial particle entrainment in a shearless mixing layer. *J. Fluid Mech.* **704**, 301–332.

IRELAND, P. J., VAITHIANATHAN, T., SUKHESWALLA, P. S., RAY, B. & COLLINS, L. R. 2013 Highly parallel particle-laden flow solver for turbulence research. *Comput. Fluids* **76**, 170–177.

https://doi.org/10.1017/jfm.2016.227 Published online by Cambridge University Press

KAWANISI, K. & SHIOZAKI, R. 2008 Turbulent effects on the settling velocity of suspended sediment. *J. Hydraul. Engng* **134**, 261–266.

LAVEZZO, V., SOLDATI, A., GERASHCHENKO, S., WARHAFT, Z. & COLLINS, L. R. 2010 On the role of gravity and shear on the acceleration of inertial particles in near-wall turbulence. *J. Fluid Mech.* **658**, 229–246.

MAXEY, M. R. 1987 The gravitational settling of aerosol particles in homogeneous turbulence and random flow fields. *J. Fluid Mech.* **174**, 441–465.

MAXEY, M. R. & RILEY, J. J. 1983 Equation of motion for a small rigid sphere in a nonuniform flow. *Phys. Fluids* **26**, 883–889.

NIELSEN, P. 1993 Turbulence effects on the settling of suspended particles. *J. Sedim. Petrol.* **63**, 835–838.

ONISHI, R., TAKAHASHI, K. & KOMORI, S. 2009 Influence of gravity on collisions of monodispersed droplets in homogeneous isotropic turbulence. *Phys. Fluids* **21**, 125108.

PAN, L. & PADOAN, P. 2010 Relative velocity of inertial particles in turbulent flows. *J. Fluid Mech.* **661**, 73–107.

PARISHANI, H., AYALA, O., ROSA, B., WANG, L.-P. & GRABOWSKI, W. W. 2015 Effects of gravity on the acceleration and pair statistics of inertial particles in homogeneous isotropic turbulence. *Phys. Fluids* **27**, 033304.

PARK, Y. & LEE, C. 2014 Gravity-driven clustering of inertial particles in turbulence. *Phys. Rev.* E **89**, 061004(R).

PINSKY, M. B., KHAIN, A. P. & SHAPIRO, M. 2007 Collisions of cloud droplets in a turbulent flow. Part IV: droplet hydrodynamic interaction. *J. Atmos. Sci.* **64**, 2462–2482.

POPE, S. B. 2000 *Turbulent Flows*. Cambridge University Press.

PRUPPACHER, H. R. & KLETT, J. D. 1997 *Microphysics of Clouds and Precipitation*. Kluwer.

READE, W. C. & COLLINS, L. R. 2000 Effect of preferential concentration on turbulent collision rates. *Phys. Fluids* **12**, 2530–2540.

REEKS, M. W. 1993 On the constitutive relations for dispersed particles in nonuniform flows. I: dispersion in a simple shear flow. *Phys. Fluids* A **5**, 750–761.

ROSA, B., PARISHANI, H., AYALA, O., GRABOWSKI, W. W. & WANG, L. P. 2013 Kinematic and dynamic collision statistics of cloud droplets from high-resolution simulations. *New J. Phys.* **15**, 045032.

SALAZAR, J. P. L. C. & COLLINS, L. R. 2012 Inertial particle acceleration statistics in turbulence: effects of filtering, biased sampling, and flow topology. *Phys. Fluids* **24**, 083302.

SHAW, R. A. 2003 Particle-turbulence interactions in atmospheric clouds. *Annu. Rev. Fluid Mech.* **35**, 183–227.

SQUIRES, K. D. & EATON, J. K. 1991 Preferential concentration of particles by turbulence. *Phys. Fluids* A **3**, 1169–1178.

SUNDARAM, S. & COLLINS, L. R. 1997 Collision statistics in an isotropic, particle-laden turbulent suspension I. Direct numerical simulations. *J. Fluid Mech.* **335**, 75–109.

SUNDARAM, S. & COLLINS, L. R. 1999 A numerical study of the modulation of isotropic turbulence by suspended particles. *J. Fluid Mech.* **379**, 105–143.

VOLK, R., CALZAVARINI, E., VERHILLE, G., LOHSE, D., MORDANT, N., PINTON, J.-F. & TOSCHI, F. 2008*a* Acceleration of heavy and light particles in turbulence: comparison between experiments and direct numerical simulations. *Physica* D **237**, 2084–2089.

VOLK, R., MORDANT, N., VERHILLE, G. & PINTON, J.-F. 2008*b* Laser Doppler measurement of inertial particle and bubble accelerations in turbulence. *Eur. Phys. Lett.* **81**, 34002.

VOßKUHLE, M., PUMIR, A., LÉVÊQUE, E. & WILKINSON, M. 2014 Prevalence of the sling effect for enhancing collision rates in turbulent suspensions. *J. Fluid Mech.* **749**, 841–852.

WANG, L.-P. & MAXEY, M. R. 1993 Settling velocity and concentration distribution of heavy particles in homogeneous isotropic turbulence. *J. Fluid Mech.* **256**, 27–68.

WANG, L.-P. & STOCK, D. E. 1993 Dispersion of heavy particles by turbulent motion. *J. Atmos. Sci.* **50**, 1897–1913.

WANG, L.-P., WEXLER, A. S. & ZHOU, Y. 2000 Statistical mechanical description and modeling of turbulent collision of inertial particles. *J. Fluid Mech.* **415**, 117–153.

https://doi.org/10.1017/jfm.2016.227 Published online by Cambridge University Press

WILKINSON, M. & MEHLIG, B. 2005 Caustics in turbulent aerosols. *Europhys. Lett.* **71**, 186–192.

WILKINSON, M., MEHLIG, B. & BEZUGLYY, V. 2006 Caustic activation of rain showers. *Phys. Rev. Lett.* **97**, 048501.

WOITTIEZ, E. J. P., JONKER, H. J. J. & PORTELA, L. M. 2009 On the combined effects of turbulence and gravity on droplet collisions in clouds: a numerical study. *J. Atmos. Sci.* **66**, 1926–1943.

YANG, C. Y. & LEI, U. 1998 The role of turbulent scales in the settling velocity of heavy particles in homogeneous isotropic turbulence. *J. Fluid Mech.* **20**, 179–205.

YANG, T. S. & SHY, S. S. 2003 The settling velocity of heavy particles in an aqueous near-isotropic turbulence. *Phys. Fluids* **15**, 868–880.

YANG, T. S. & SHY, S. S. 2005 Two-way interaction between solid particles and homogeneous air turbulence: particle settling rate and turbulence modification measurements. *J. Fluid Mech.* **526**, 171–216.

YUDINE, M. I. 1959 Physical considerations on heavy-particle dispersion. *Adv. Geophys.* **6**, 185–191.

ZAICHIK, L. I. & ALIPCHENKOV, V. M. 2008 Acceleration of heavy particles in isotropic turbulence. *Intl J. Multiphase Flow* **34** (9), 865–868.

ZAICHIK, L. I. & ALIPCHENKOV, V. M. 2009 Statistical models for predicting pair dispersion and particle clustering in isotropic turbulence and their applications. *New J. Phys.* **11**, 103018.

https://doi.org/10.1017/jfm.2016.227 Published online by Cambridge University Press